

Spring 2012

Design and Implementation of a Z-Axis MEMS Gyroscope with a Symmetric Multiple-Mass Mechanical Structure

Yujie Zhang
Old Dominion University

Follow this and additional works at: https://digitalcommons.odu.edu/mae_etds



Part of the [Applied Mechanics Commons](#), and the [Electrical and Computer Engineering Commons](#)

Recommended Citation

Zhang, Yujie. "Design and Implementation of a Z-Axis MEMS Gyroscope with a Symmetric Multiple-Mass Mechanical Structure" (2012). Master of Science (MS), Thesis, Mechanical & Aerospace Engineering, Old Dominion University, DOI: 10.25777/f5vj-gk54
https://digitalcommons.odu.edu/mae_etds/164

This Thesis is brought to you for free and open access by the Mechanical & Aerospace Engineering at ODU Digital Commons. It has been accepted for inclusion in Mechanical & Aerospace Engineering Theses & Dissertations by an authorized administrator of ODU Digital Commons. For more information, please contact digitalcommons@odu.edu.

**DESIGN AND IMPLEMENTATION OF A Z-AXIS MEMS GYROSCOPE WITH
A SYMMETRIC MULTIPLE-MASS MECHANICAL STRUCTURE**

by

Yujie Zhang
B.S. July 2010, Shenyang University of Science and Technology, China

A Thesis Submitted to the Faculty of
Old Dominion University in Partial Fulfillment of the
Requirements for the Degree of

MASTER OF SCIENCE

MECHANICAL ENGINEERING

OLD DOMINION UNIVERSITY
May 2012

Approved by:

Zhili Hao (Advisor)

Han Bao (Member)

Colin Britcher (Member)

ABSTRACT

DESIGN AND IMPLEMENTATION OF A Z-AXIS MEMS GYROSCOPE WITH A SYMMETRIC MULTIPLE-MASS MECHANICAL STRUCTURE

Yujie Zhang
Old Dominion University, 2012
Advisor: Dr. Zhili Hao

This thesis presents a z-axis MEMS gyroscope with a symmetric mechanical structure. The multiple-mass design prioritizes the sense-mode Quality Factor (Q) and thus improves its scale factor. The proposed mechanically coupled, dynamically balanced anti-phase sense-mode design minimizes energy dissipation through the substrate in order to maximize the Q. Numerical simulation is implemented in a finite element analysis software, COMSOL, to identify the two operation modes of the gyroscope: drive-mode and sense-mode. The multiple-mass gyroscope design is further fabricated using a one-mask process. Experimental characterization of frequency response in both drive-mode and sense-mode of the device are conducted, proving the design concept for improving the Q in the sense-mode.

This thesis is dedicated to my parents and my wife.

ACKNOWLEDGMENTS

First I would like to present my gratitude to Dr. Zhili Hao, who has been my academic advisor during the past two years. I am grateful to her for providing me the great opportunity to study MEMS technology, for offering all the academic resources and for sharing the idea of creating. Her extensive knowledge and graceful academic attitude have guided me throughout the course of my research work.

I would like to thank Dr. Gene Hou for his continuous support in my graduate research. Also, many thanks go to Diane Mitchell and June Blount for all their administrative help.

I would like to express my appreciation to Dr. Han Bao for showing his interest in my thesis research. I would like to thank Dr. Colin Britcher for his great help on the thesis editing.

I would like to give my special thanks to my fellow group members: Ren Wang, Peng Cheng, Fei Xie and Wenting Gu. Their help benefit me both academically and socially. The home-like atmosphere makes the research work easier.

Last but not least, I would like to present my deepest gratitude to my parents and my wife, it is their love and support that make me who I am today and who I will be in the future.

NOMENCLATURE

C_0 :	Static sense capacitance, F
D:	Damping factors, (Dimensionless)
d_d :	Gap between two opposite comb-fingers, μm
F_d :	Electrostatic force applied on the drive electrodes, N
F_c :	Coriolis force, N
f_s :	Sense-mode frequency, kHz
f_d :	Drive-mode frequency, kHz
h:	Structure thickness, μm
K:	Spring constant, N/m
K_s :	Mechanical stiffness along the sense-mode direction, N/m
K_e :	Electrostatic stiffness, N/m
m:	Weight of the mass, g
m_c :	Mass that sensitive to the Coriolis force, g
M:	Effective mass of the TFG, g
n:	Number of the fingers of the comb-drive electrodes, (Dimensionless)
Q:	Quality factor, (Dimensionless)
Q_s :	Sense-mode Quality factor, (Dimensionless)

V_d :	Driving AC voltage, V
\vec{V}_x :	X-axis velocity, m/s
V_p :	Polarization voltage, V
\dot{x} :	Drive-mode vibration amplitude, μm
X :	Axial displacement of the proof mass, μm
y_0 :	Mechanical gain, (Dimensionless)
$\vec{\Omega}_z$:	Rotation rate along z-axis, deg/s
ω_n :	Angular frequency, rad/s
ω_d :	Drive-mode angular frequency, rad/s
ϕ_d :	Drive-mode position phase, deg
ϕ_s :	Sense-mode position phase, deg
ϵ_0 :	Permittivity of the free space, F/m

TABLE OF CONTENTS

	Page
LIST OF TABLES	X
LIST OF FIGURES	XI
 Chapter	
1 INTRODUCTION TO MEMS GYROSCOPES	1
1.1 Applications of MEMS Gyroscopes	1
1.2 Coriolis Effect.....	3
1.3 Current Technical Issues Associated with Tuning-Fork Gyroscope	6
1.3.1 Mode Mismatch	8
1.3.2 Demand for Larger Operation Bandwidth	9
1.3.3 Mechanical Sensitivity and Coriolis Response	10
1.4 Motivation.....	12
1.5 Thesis Organization	12
 2 DESIGN OF A Z-AXIS MEMS GYROSCOPE	 14
2.1 Overview of a Developed Multiple-Beam Tuning-Fork Gyroscope	14
2.2 New Design Concept	18
2.3 Design Configuration Type I	19
2.3.1 Drive-Mode Design.....	20
2.3.2 Sense-Mode Design	23
2.4 Design Configuration Type II.....	26
2.5 Finite Element Method Simulation.....	28
 3 FABRICATION PROCESS	 34
3.1 Fabrication Procedure	34
3.2 Fabrication Imperfections	38
 4 EXPERIMENTAL CHARACTERIZATION	 41
4.1 Electromechanical System Level Model	41

	Page
4.2 Experimental Setup for Q Measurement.....	44
4.3 Testing Results and Discussions.....	46
5 CONCLUSIONS AND FUTURE DIRECTIONS.....	49
5.1 Summary of the Research Work	49
5.2 Future Direction.....	49
REFERENCES	51
VITA.....	54

LIST OF TABLES

Table	Page
2.1: Simulation result of the TFG shows the frequency and mode order	33
3.1: Basic electrical analogy and equivalent quantities	35
3.2: Frequency response measurement result for the designated device	42
4.1: Key parameters of the TFG	47

LIST OF FIGURES

Figure	Page
1.1: A MEMS gyroscope from STMicroelectronics.....	3
1.2: Tuning fork physics	4
1.3: The scanning electron micrograph of the first tuning-fork gyroscope from the Draper Laboratory.....	5
1.4: A gyroscope fabricated by the Micro-Device & Micromechanics Lab at Old Dominion University in 2009	5
2.1: SEM picture of the multiple-beam tuning-fork gyroscope (MB-TFG) [16]	15
2.2: Drive-mode oscillation and its normal stress.....	17
2.3: Sense-mode oscillation	18
2.4: Simulation of the surface traction of the anchor shows the evidence of unbalanced torque from the sense-mode.....	18
2.5: Structural schematic view of the proposed gyroscope architecture for maximization of the sense-mode quality factor. Picture (a) Shows drive-mode configuration and (b) shows the sense-mode configuration.	20
2.6: Signal configuration of the drive-mode and sense-mode vibration behavior	21
2.7: Lumped model of the TFG in the drive-mode.....	22
2.8: DRIE fabricated parallel-plate sense electrode.....	24
2.9: A schematic view of the parallel-plate electrostatic actuator	25
2.10: (a) Drive-mode motion and (b) Sense-mode motion	27
2.11: FEM simulation results of the TFG	32
3.1: Mask drawing for the TFG	34
3.2: Fabrication process of the TFG	36
3.3: SEM picture of the fabricated TFG	37

Figure	Page
3.4: Sensing gap configuration	38
3.5: DRIE over-etching.....	39
3.6: HF over-etching under the anchor	40
4.1: Equivalent electrical circuit model for a two port MEMS resonator.....	41
4.2: Schematic view of the two port resonator with parallel-plate (left) electrodes and comb-drive electrodes (right).	43
4.3: Schematic view of experimental setup	45
4.4: Testing equipment and setup	46
4.5: Measured frequency response for Device #2 and #4.....	48

CHAPTER 1

INTRODUCTION TO MEMS GYROSCOPES

A traditional gyroscope is a device for measuring and maintaining rotation and orientation. Recent developed gyroscopes also have the function of measuring the rate of rotation [1]. The working principle of the traditional gyroscope depends on conservation of angular momentum and is designed to spin with any orientation. The spinning wheel and disk structure widely used for such prototypes would inevitably induce bearing friction and wear [2]. In order to avoid friction and wear problem of the traditional gyroscope, vibrating gyroscope was presented as an effective solution by eliminating most of the rotating structures. Other high-performance gyroscopes, such as Fiber-Optic Gyroscope and Ring Laser Gyroscope, which can completely eliminate friction are also developed [3]. These optical gyroscopes are not widely used in low-end applications due to their extremely high cost and thus will not be discussed in detail in this article. Micro Electro Mechanical System (MEMS) gyroscopes on the other hand, were found to have many advantages over both vibration gyroscopes and optical gyroscopes such as low cost, small size and low energy consumption [2].

1.1 Applications of MEMS Gyroscopes

With the development of semiconductor fabrication technology, almost any two dimensional mechanical structure can be batch-produced on silicon wafers and packaged with integrated circuits. Consequently, inexpensive MEMS vibration gyroscopes have been greatly developed in the past 30 years [4]. Because of their high stability, high

performance-cost ratio, low power consumption and small size, they are widely used in space navigation, consumer electronics, medical applications and the automotive industry.

For military applications, gyroscopes are an integral part of the Inertial Measurement Units (IMU) and Inertial Navigation Systems (INS) [5, 6]. In the inertial reference frame, gyroscopes provide the angular velocity information of the system by comparing its current and original orientation. This process is just like when a blindfolded passenger in the car knows the direction of the car by comparing the situation a moment before the movement [6].

For consumer electronics, MEMS gyroscopes and accelerometers are installed on devices like smartphones, tablets and play-stations to collect the heading information, which is, position and orientation. Take Nintendo Wii as an example, the movement of the player can be decomposed as rotation and acceleration, which are respectively detected by the MEMS gyroscopes and accelerometers inside the controller. Instantly, this information is being processed by microprocessors so that the motion of the player can be mapped on the TV. In the automotive industry, MEMS gyroscopes are used for anti-skid control, rollover detection, air-bag sensing system, Anti-Lock Brake System (ABS) and Global Positioning System (GPS). Those gyroscopes are assigned to three different axis (pitch, roll and yaw) to monitor the real-time dynamical motion of the car. Fig. 1.1 shows a MEMS gyroscope installed in a car.



Figure 1.1: A MEMS gyroscope from STMicroelectronics

1.2 Coriolis Effect

To illustrate the working principle of a typical tuning-fork gyroscope (TFG), one should introduce the Coriolis Effect first. In the example of a simple tuning fork, as shown in Fig. 1.2 [7], the tines of the tuning fork are stimulated to resonate along the x-axis with velocity \vec{V}_x at certain amplitude and we call this vibration mode the drive-mode. When the tuning fork rotates along the z-axis with a rotation rate of $\vec{\Omega}_z$, the Coriolis Effect induces a force perpendicular to the tines of the tuning fork with the acceleration equals to $-2\vec{\Omega}_z \times \vec{V}_x$. This force causes the deflection of the tines along the y-axis and we call this vibration mode the sense-mode [7]. The Coriolis force is proportional to the applied angular rate from which the displacement can be measured in a capacitive fashion [8]. Electrostatic, electromagnetic, or piezoelectric mechanisms can also be used to detect this force.

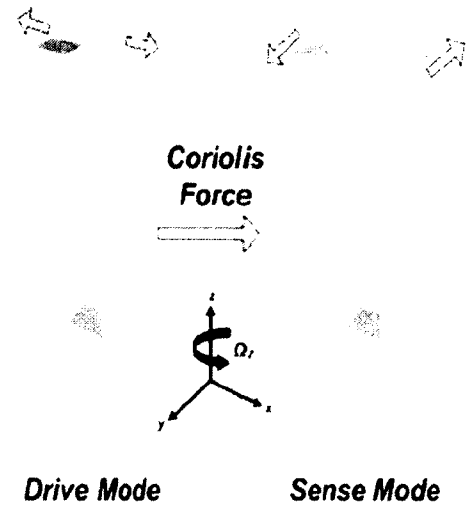
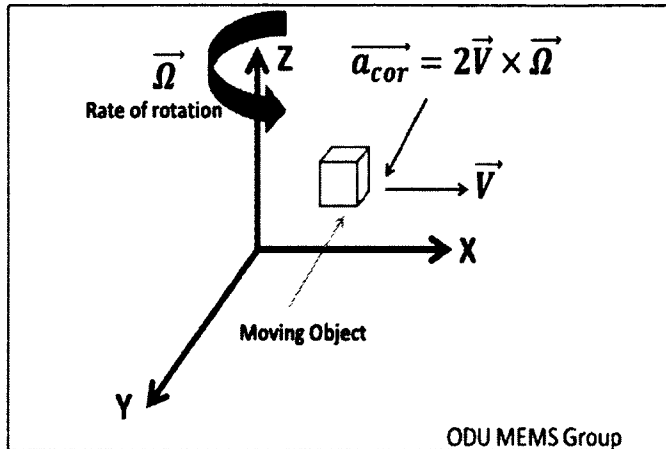


Figure 1.2: Tuning fork physics

Based on the Coriolis Effect, the first MEMS tuning-fork gyroscope (as shown in Fig. 1.3) was designed and fabricated by Draper Laboratory in 1993 [9]. A considerable amount of work was done by researchers to improve the performance of this prototype of gyroscope. Fig. 1.4 shows a more recent generation tuning-fork gyroscope and it was fabricated by the Micro-Device & Micromechanics Lab at Old Dominion University in 2009. The detailed working principle of this tuning-fork gyroscope is covered in the following chapters.

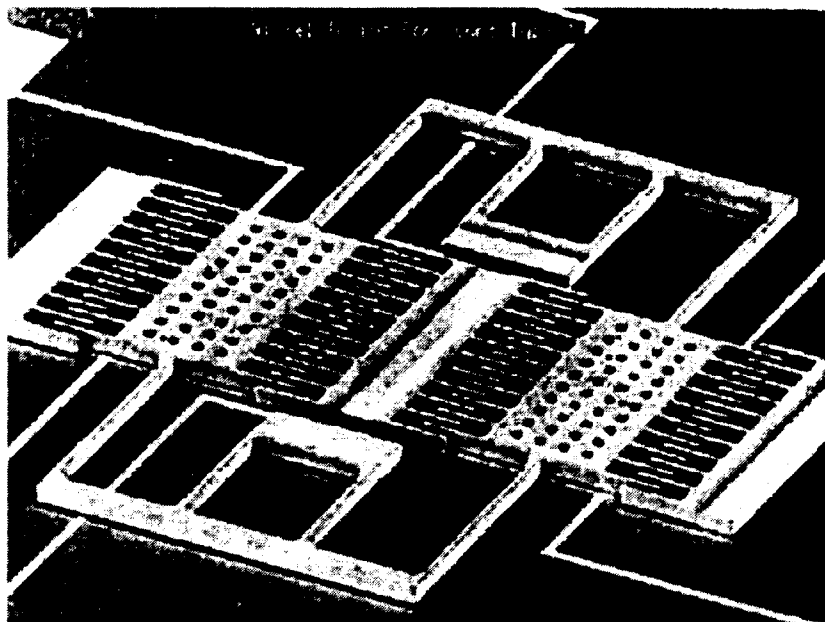


Figure 1.3: The scanning electron micrograph of the first tuning-fork gyroscope from the Draper Laboratory

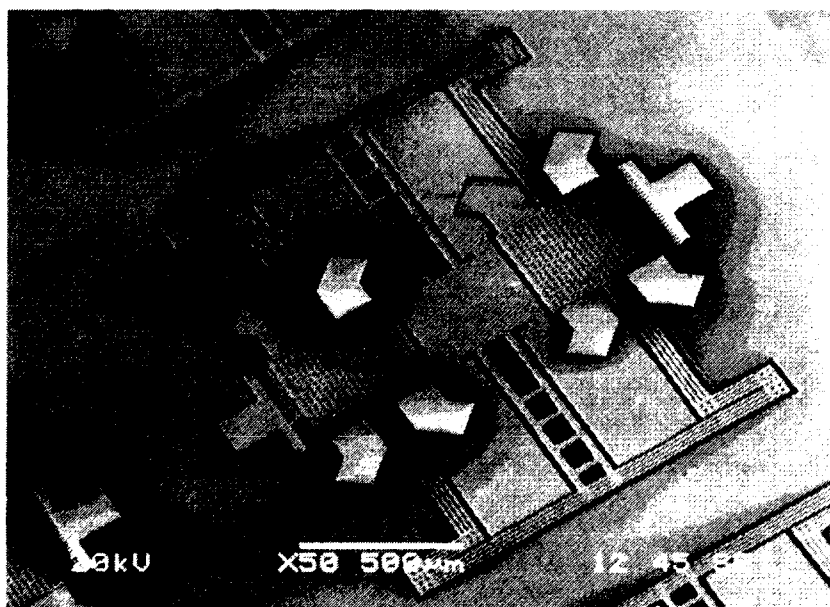


Figure 1.4: A gyroscope fabricated by the Micro-Device & Micromechanics Lab at Old Dominion University in 2009

1.3 Current Technical Issues Associated with Tuning-Fork Gyroscope

Three major challenges that face gyroscope designers are mechanical sensitivity, operation bandwidth and robustness against environment variation [10]. There are several key parameters to describe the performance of a MEMS gyroscope. From the IEEE Standard for Inertial Sensor Terminology [11], those key parameters include: rate sensitivity, bias (zero rate output), operation range (input rate limits), resolution, bandwidth, turn-on time, linear and angular vibration sensitivity, shock resistance and quality factor.

(1) Rate sensitivity: the ratio of the change in output to the change of the input intended to be measured, typically specified in mV/deg /sec.

(2) Bias: the average over a specified time of gyro output measured at specified operating conditions that have no correlation with input rotation.

(3) Operating range: range of positive and negative angular rates that can be detected without saturation.

(4) Resolution: the largest value of the minimum change in input, for inputs greater than the noise level, which produces a change in output equal to some specified percentage (more than 50%) of the change in output, expected using the nominal scale factor.

(5) Bandwidth: the range of frequency of the angular rate input that the gyroscope can detect. Typically specified as the cutoff frequency coinciding to the -3dB point.

(6) Quality factor (Q): it is defined as the maximum ratio of the amplitude to the static deflection, which is F/K . If the system is a lightly damped system, the Q can be written as:

$$Q = \frac{m\omega_n}{c} \quad (1.1)$$

Among these parameters, one may be proportional to the reciprocal of another and such a relationship forces researchers to consider the tradeoffs when designing a new gyroscope. For instance, quality factor and bandwidth is one pair of tradeoffs. From Equation 1.2, the quality factor is found to be inversely proportional to the bandwidth of the system. Larger quality factor can be achieved either by decreasing the system damping, or by further merging the two natural frequencies, both of which would lower the operational bandwidth [11]. Taking a specific research work as an example, in the year 2007, Georgia Institute of Technology demonstrated a tuning-fork gyroscope which has a quality factor of 40,000 with a bandwidth of 0.4Hz. On the contrast, the quality factor of the same device will drop to only 10,000 when the bandwidth reaches 2Hz [12]. This work shows that if there was a small mode mismatch between the sense-mode and drive-mode, in another word, larger bandwidth, the quality factor will drop very fast.

$$BW \approx \frac{\omega_n}{Q} \quad (1.2)$$

However, researchers can make their decisions among these tradeoffs by considering the specific application of the gyroscope. In gyrocompass navigation, where high rate resolution is important, hence, high quality factor has the priority, so a small bandwidth is tolerable. Conversely, in other cases such as the car roll-over situation where high yaw

rates need to be detected, minimum response time of the gyroscope system is crucial and therefore a larger bandwidth is required [12].

1.3.1 Mode Mismatch

Previous research work demonstrates that a higher bandwidth will induce a reduction of quality factor in both sense-mode and drive-mode. In order to maximize the quality factor, researchers attempted to design the gyroscope with perfect or near perfect mode-match, in other words, minimum separation between the two natural frequencies. The resonance frequencies of both modes are mainly determined by the stiffness of the beams, which relate to the material property as well as the beam length and width. In the design process, the dimensions of the beams are designed to be some specific values which satisfy mode-match requirement. Due to fabrication imperfection and environmental variation (such as temperature variation and humidity variation), separation of frequencies between the sense-mode and drive-mode are hard to avoid. Researchers then come up with a method to manually tune the resonant frequency in the sense-mode close to the resonant frequency in the drive-mode. The following shows the detailed explanation of the electrostatic tuning method. The resonant frequency in the sense-mode is given as:

$$f_s = \frac{1}{2\pi} \sqrt{\frac{K_s - K_e}{M}} \quad (1.3)$$

In this equation, K_s denotes the mechanical stiffness of the sense direction while K_e represents the electrostatic stiffness along the sense axis. Increasing the polarization voltage V_p can lower the sense-mode frequency, while the drive-mode frequency is

relatively independent of the polarization voltage change since the drive-mode oscillation is excited by comb-drive electrodes, hence, no electrostatic stiffness [19]. Depend on the statement above, the sense-mode resonant frequency is usually designed to be slightly larger than the drive-mode resonant frequency, which leaves a space for the frequency tuning process to compensate the mode-mismatch problem caused by fabrication imperfections.

Even though the sense-mode frequency can be tuned close to the drive-mode frequency by increasing V_p , some research work proved that a higher V_p will cause an increase of the Thermo-Elastic Damping (TED), which would lead to a drop of the quality factor. Meanwhile, if the two vibration modes were tuned to be very close, it would also affect the sensor's robustness, temperature drift and linear operation range [7].

1.3.2 Demand for Larger Operation Bandwidth

Most of the real world applications, such as the automotive industry and consumer electronics, desired the bandwidth of the gyroscope to be above 100Hz, but no more than 400Hz. A mode-matched gyroscope which has a 1Hz bandwidth would typically have a quality factor of 10,000 at a 10kHz resonant frequency. It is obvious that the mode matching gyroscope can only satisfy the high sensitivity requirement, but not for the large operational range. Research work has been done to improve the operational bandwidth by introducing multiple Degree of Freedom (DOF) dynamic sense-mode architecture. In 2008, the research group in the University of California at Irvine and the Middle East Technical University at Ankara presented two multiple DOF sense-mode gyroscopes with operational bandwidth of 250 Hz [13] and 1000 Hz [14], respectively.

1.3.3 Mechanical Sensitivity and Coriolis Response

The sensitivity, as known as scale factor, of a gyroscope is the ratio of the change in the output to a unit change in the input that is to be measured. It measures how sensitive the device is in response to an input rotation rate signal [15]. The following equations are discussed to illustrate the mechanical sensitivity and Coriolis response in a mathematical way. In Equation 1.4, the vibration amplitude of the drive-mode can be described as:

$$\dot{x} = x_0 \sin(\omega_d t + \phi_d) \quad (1.4)$$

In this form, ω_d denotes the drive-mode resonant frequency, x_0 is a constant and ϕ_d is the drive-mode position phase relative to the drive AC signal. In most cases, the drive-mode oscillation is driven into resonance so that ϕ_d becomes -90° . On the other hand, the sense-mode oscillation is excited by Coriolis force F_c , which is given by

$$F_c = -2m_c \Omega_z \dot{x} = -2m_c \Omega_z \omega_d x_0 \sin(\omega_d t + \phi_d) \quad (1.5)$$

Where m_c denotes the mass that sensitive to the Coriolis force. In a single mass or symmetrical gyroscope structure, all of the mass/masses is/are being used to sense the Coriolis force so as to improve the sensitivity. Conceptually, a gyroscope can be simply regarded as a one degree of freedom oscillator so that the governing equation can be written as:

$$m_s \ddot{y} + c_s \dot{y} + k_s y = -2m_c \Omega_z x_0 \omega_d \sin(\omega_d t + \phi_d) \quad (1.6)$$

where m_s is the mass that sensitive to the Coriolis force. By defining the sense-mode resonant frequency ω_s and the sense-mode quality factor Q_s :

$$\omega_s = \sqrt{\frac{K_s}{m_s}} \quad (1.7)$$

$$Q_s = \frac{m_s \omega_s}{c_s} \quad (1.8)$$

the mechanical gain of the sense-mode can be shown as:

$$y_0 = \Omega_z \frac{m_c \omega_d}{m_s \omega_s^2} \frac{2x_0}{\sqrt{\left[1 - \left(\frac{\omega_d}{\omega_s}\right)^2\right]^2 + \left[\frac{1}{Q_s} \frac{\omega_d}{\omega_s}\right]^2}} \quad (1.9)$$

Intuitively, for a given input rotation rate, larger deflection in the sense-mode causes larger change in the sense capacitances, generating larger electrical output which leads to higher sensitivity. As stated above, the drive-mode and sense-mode frequencies are generally designed to be very close to each other to achieve the maximum sensitivity. Such a situation reduces the sense-mode vibration amplitude to:

$$y_{0_{res}} = \Omega_z \frac{2Q_s x_0 m_c}{m_s \omega_s} \quad (1.10)$$

Equation 1.10 shows several ways of improving the sense-mode vibration amplitude so as to increase the sensitivity of the gyroscope. For example, by increasing the drive-mode oscillation amplitude x_0 and maximizing the quality factor in the sense-mode through reducing energy dissipation. Some of these optimization methods will be covered in the following chapters.

1.4 Motivation

By analyzing the technical issues of the current developed tuning-fork gyroscope, we observed that the quality factor in the sense-mode is critical for the overall performance of the gyroscope. High quality factor in the sense-mode directly amplifies the vibration amplitude and thus improves the scale factor. Previously designed gyroscopes usually show a large quality factor in the drive-mode and a relatively small quality factor in the sense-mode [7]. This is because the drive-mode oscillation operates in the linearly coupled, anti-phase resonant mode, which balances both linear momentum as well as moment of reaction forces, so that the energy dissipation through the substrate is effectively eliminated. By contrast, despite the fact that linear momentum is balanced in sense-mode, the moment of reaction force is not well balanced. As a result, to seek an effective method which could increase the quality factor in the sense-mode serves as the motivation of the research work done by this thesis.

1.5 Thesis Organization

The remainder of this thesis is organized as follows. Chapter 2 presents the design of the tuning-fork gyroscope with a symmetric 2-DOF mechanical structure. It also provides the detailed explanation of the gyroscope's operation principle, performance specifications and theoretical analysis. Design challenges such as mode order and mode shape are also elaborated.

Chapter 3 focuses on the fabrication process of the tuning-fork gyroscope. One mask is used to characterize the Silicon on Isolator (SOI) wafer. Deep Reactive Ion Etching (DRIE) and Hydrofluoric (HF) acid etching are discussed.

Chapter 4 discusses the experimental work for characterizing the frequency response of the fabricated gyroscope. Experimental setup and procedures are discussed in detail. The experimental data is examined as well.

Chapter 5 concludes this work with an overview of the contributions of this research and proposes possible future direction in performance optimization of this tuning-fork gyroscope.

CHAPTER 2

DESIGN OF A Z-AXIS MEMS GYROSCOPE

This chapter starts with analyzing the advantages and disadvantages of the previous generation tuning-fork gyroscope, and then presents the design configuration of the optimized new tuning-fork gyroscope. Theoretical analysis and FEM simulation of the design are followed.

2.1 Overview of a Developed Multiple-Beam Tuning-Fork Gyroscope

Based on the Coriolis Effect, a MEMS multiple-beam tuning-fork gyroscope (MB-TFG) was designed and fabricated by the MEMS group at Old Dominion University in 2009 [16]. Fig. 2.1 shows a SEM picture of the MB-TFG.

This multiple-beam mechanical structure consists of an anchor, two proof masses and a flexural structure of four beams in parallel. The whole structure is fixed on the substrate through the anchor located at its center. Dual proof masses are symmetrically located on both sides of the anchor to form the vibrating portion of the gyroscope. Four parallel-plate sensing electrodes and four tuning electrodes are distributed around the proof masses with the purpose of capacitive sensing and frequency tuning, respectively. Comb-drive electrodes are placed on both sides of the proof masses for electrostatic actuation.

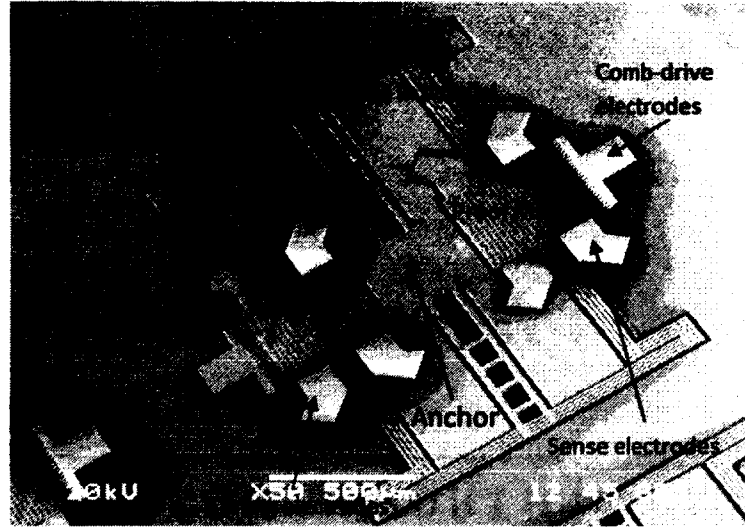


Figure 2.1: SEM picture of the multiple-beam tuning-fork gyroscope (MB-TFG) [16]

The working principle of this multiple-beam tuning-fork gyroscope is based on the energy transfer from one vibration mode to another: one along x-axis (drive-mode) and the other along the y-axis (sense-mode). When operating, the two proof masses are first driven into harmonic motion at their resonant frequency along x-axis by the comb-drive electrodes, while a rotation rate signal, Ω_z , induces a Coriolis Acceleration along the y-axis and excites the in-plane vibrations in the sense-mode. The vibration of the sense-mode is then detected by the parallel-plate sensing electrodes.

In reviewing of this tuning-fork gyroscope, it is designed with an operational frequency between 10kHz to 20kHz to avoid any environmental noise and keep the operational voltage at a relatively low level. One of the limitations of this tuning-fork gyroscope is its relatively low quality factor in the sense-mode (100k), which is only half of the quality factor in the drive-mode (200k). As mentioned before, quality factor is one of the most important parameters since it is closely related to several key performance

specifications of a gyroscope. In short, quality factor represents the damping level of the system. High quality factor means the system has a less energy dissipation, in other words, not energy efficient [17].

Regarding this gyroscope, the energy loss mechanisms mainly include anchor loss, surface loss, Thermal-Elastic Damping (TED), air damping and intrinsic damping. The overall quality factor of a gyroscope is based on the sum of these losses [18, 19].

$$\frac{1}{Q_{\text{measured}}} = \frac{1}{Q_{\text{TED}}} + \frac{1}{Q_{\text{anchor loss}}} + \frac{1}{Q_{\text{surface}}} + \frac{1}{Q_{\text{air damping}}} + \frac{1}{Q_{\text{intrinsic}}} \quad (2.1)$$

where Q_{TED} , $Q_{\text{anchor loss}}$, Q_{surface} , $Q_{\text{air damping}}$ and $Q_{\text{intrinsic}}$ denote the quality factor related to TED, anchor loss, surface loss, air damping and intrinsic loss. Among those five damping sources, air damping can be ignored since the gyroscope is operated in a vacuum environment. Surface loss can be made negligible through optimized processing. Intrinsic loss of silicon is very high so that the reciprocal of it become negligible. From the above analysis, TED and anchor loss are the two dominant energy loss sources of this gyroscope [19].

Anchor loss is caused by the reaction force at the clamped region of a mechanical structure during vibration. The relatively small anchor loss in the drive-mode comes from the anti-phase, dynamically balanced motion of the proof masses, while the relatively large anchor loss in the sense-mode is due to the net torque applied on the anchor by the unsymmetrical motion of the proof masses.

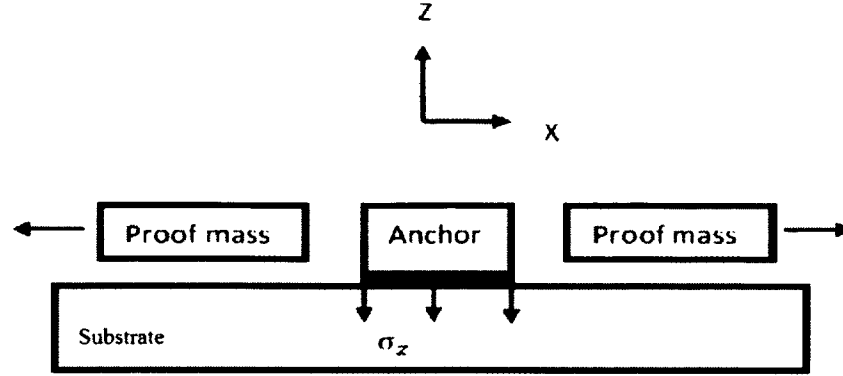


Figure 2.2: Drive-mode oscillation and its normal stress

As shown in Fig. 2.2, since there is no net force applied on the anchor, the quality factor related to anchor loss in the drive-mode is expected to be well above 9×10^{15} [18]. In comparison, as shown in Fig. 2.3, the quality factor related to anchor loss in the sense-mode is expected to be much smaller than its counterpart in the drive-mode. By modeling the surface traction of the anchor in the sense-mode, the stress concentration region is being exposed. Fig. 2.4 shows the FEM simulation result of the anchor in the sense-mode, where mechanical energy of the gyroscope irreversibly transfers into other types of energy which are easier to be dissipated.

In conclusion, the relatively low quality factor in the sense-mode is due to the large net torque applied on the anchor. In order to resolve this problem, a new design concept which would reduce the anchor loss is being introduced in the following paragraphs.

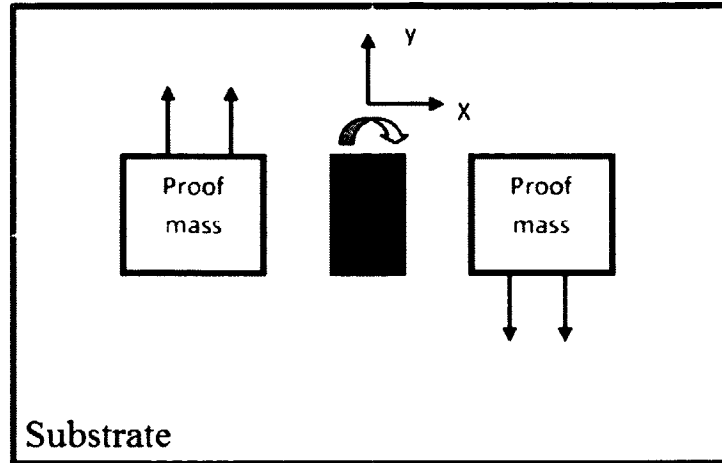


Figure 2.3: Sense-mode oscillation

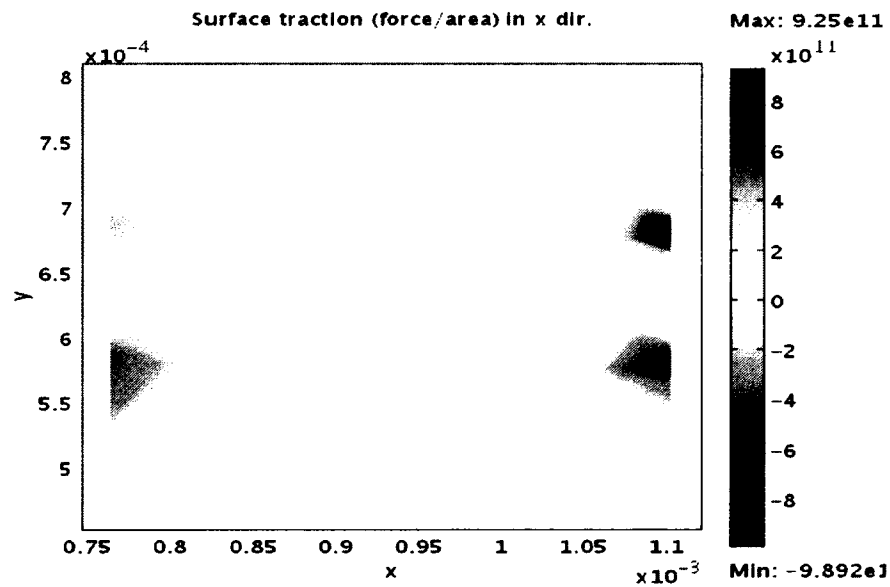


Figure 2.4: Simulation of the surface traction of the anchor shows the evidence of unbalanced torque from the sense-mode

2.2 New Design Concept

Based on the above analysis, one way to increase the sense-mode quality factor is by alleviating the anchor loss. Thus, a new design optimization was recently done, which focuses on minimizing the unbalanced torque in the sense-mode of the conventional

design. Unlike previous tuning-fork implementations, the proposed architecture adds another proof mass on each side of the original proof masses, which balances both linear momentum and torque in the sense-mode, hence, lower the anchor loss. The energy dissipation through the substrate is effectively eliminated.

2.3 Design Configuration Type I

The proposed mechanical architecture, as shown in Fig. 2.5, comprises four proof masses, a flexural structure of multiple beams and a centrally located anchor. A pair of comb-finger electrodes, eight parallel-plate sense electrodes, and eight tuning electrodes are employed to operate the gyroscope. This 2-DOF mechanical structure keeps the vibration along x-axis as the drive-mode and y-axis as the sense-mode. In the drive-mode, which is illustrated in Fig. 2.5 (a), the four proof masses are driven into harmonic motion along x-axis at the same time, but in different directions. In the examination of the sense-mode, as shown in Fig. 2.5 (b), the rotation rate signal induced Coriolis Acceleration applies on the four proof masses so as to switch their vibration directions. The very left proof mass and the third proof mass vibrate at the same direction while the second proof mass and the very right proof mass move toward the same direction, but opposite to the first pair. By assigning this particular type of motion, the net torque generated by the two proof masses on the left of the anchor is completely balanced by its counterpart on the right.

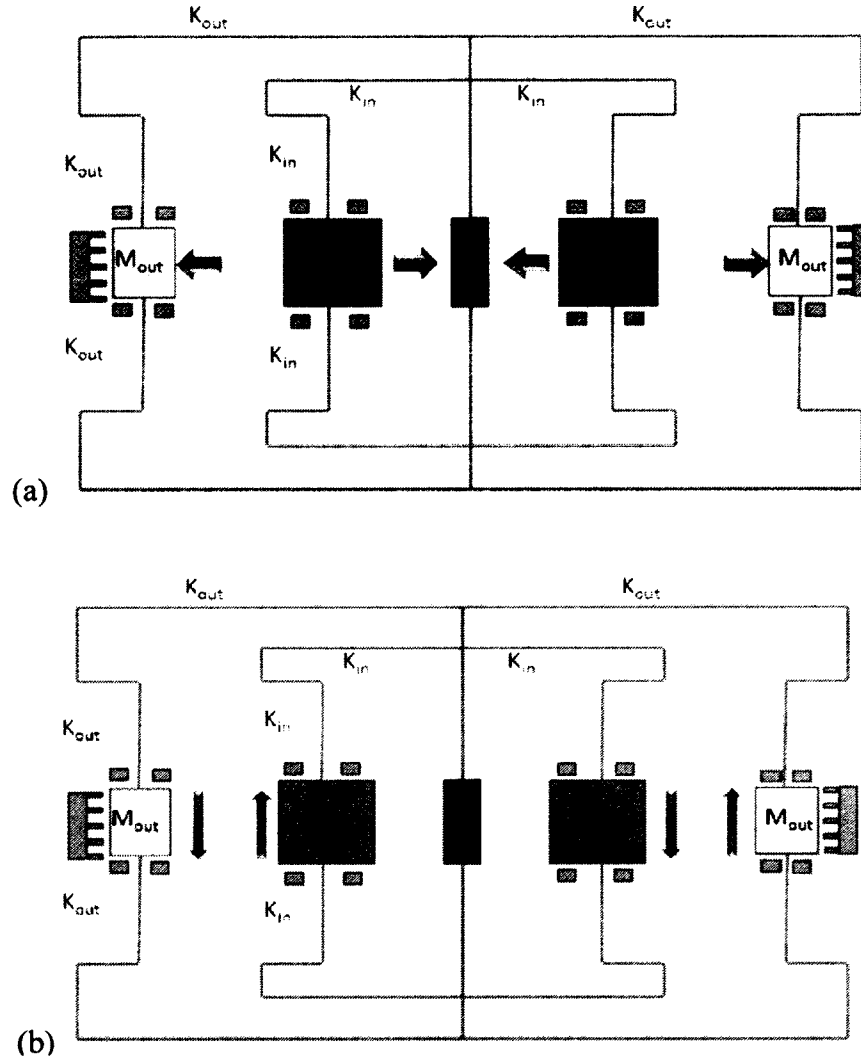


Figure 2.5: Structural schematic view of the proposed gyroscope architecture for maximization of the sense-mode quality factor. Picture (a) Shows drive-mode configuration and (b) shows the sense-mode configuration.

2.3.1 Drive-Mode Design

The drive-mode motion of the proposed architecture is driven by comb-finger electrodes. For the comb-drive electrodes, one comb structure is fixed while the other one is mobile. When operating, as shown in Fig. 2.6, a polarization voltage V_p is applied on the anchor, hence, the mobile comb-drive electrodes. At the same time, a AC signal is applied one

side of the fixed comb-drive electrode to establish the drive-mode vibration, and output current is generated and detected by the fixed comb-drive electrode on the other side [20].

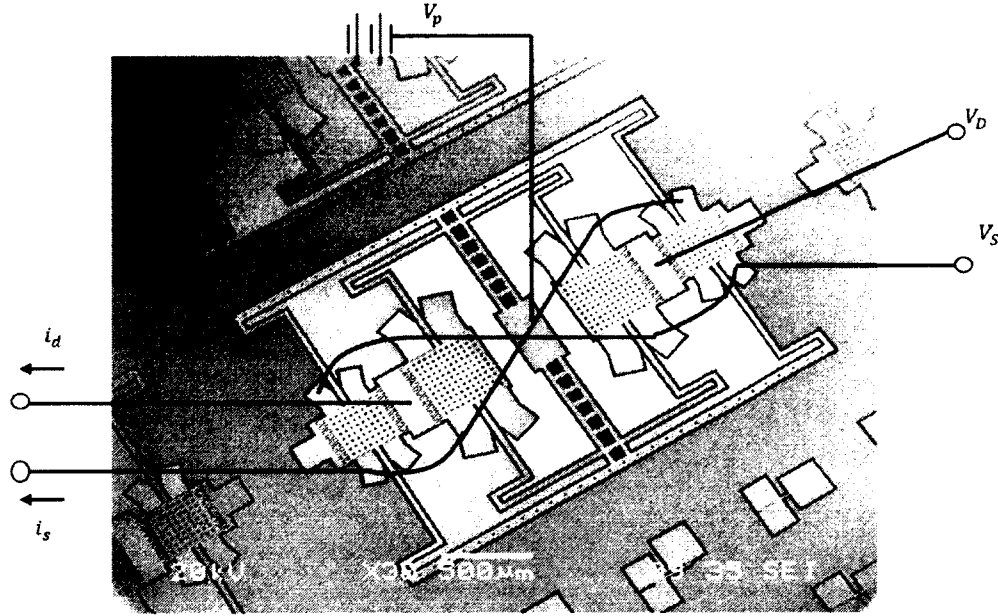


Figure 2.6: Signal configuration of the drive-mode and sense-mode vibration behavior

As discussed above, the movement of the proof masses rely on the electrostatic force generated by the change of the overlapping capacitive area of the two opposite comb fingers, as shown in Equation 2.2 [21]

$$F_d = n\epsilon_0(V_p - V_d)^2 \frac{h}{d_d} \quad (2.2)$$

where ϵ_0 is the permittivity of free space, n is the number of fingers on the electrodes, h is the thickness and d_d is the gap between two opposite comb-fingers.

In the drive-mode, there are two proof masses on each side of the anchor so that we can consider its lumped element model as a 2-DOF mass-spring-damper system. The schematic view of the equivalent lumped element model is illustrated in Fig. 2.7, where X_1 and X_2 are the axial displacement of the two proof masses, M_1 and M_2 are the effective masses of the TFG, D_{d1} and D_{d2} , D_{d3} are the damping factors in the drive-mode, K_{d1} and K_{d2} , K_{d3} are the effective mechanical stiffness of the flexural beams.

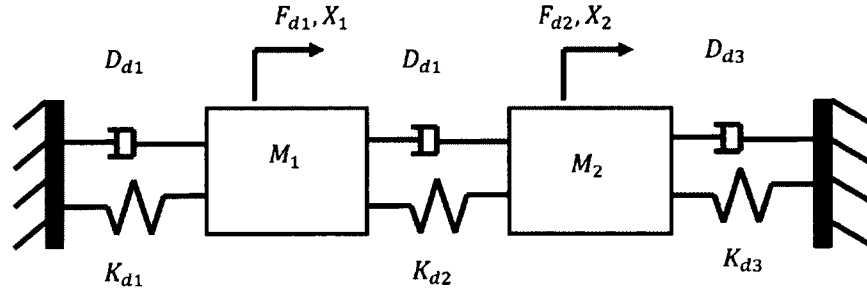


Figure 2.7: Lumped model of the TFG in the drive-mode

The second-order ordinary differential equation (ODE) that governs the dynamic behavior of the system is given by:

$$[M]\ddot{X} + [C]\dot{X} + [K]X = F \quad (2.3)$$

where

$$M = \begin{bmatrix} M_1 & 0 \\ 0 & M_2 \end{bmatrix} \quad (2.4)$$

$$C = \begin{bmatrix} D_{d1} + D_{d2} & -D_{d2} \\ -D_{d2} & D_{d2} + D_{d3} \end{bmatrix} \quad (2.5)$$

$$K = \begin{bmatrix} K_{d1} + K_{d2} & -K_{d2} \\ -K_{d2} & K_{d2} + K_{d3} \end{bmatrix} \quad (2.6)$$

$$F = \begin{bmatrix} F_{d1} \\ F_{d2} \end{bmatrix} \quad (2.7)$$

As mentioned before, comb-drive electrodes are employed in the drive-mode to provide the electrostatic forces which drive the proof masses into vibration. The driving forces applied on the proof masses are given by:

$$F_{d1} = 2n_1\epsilon_0 \frac{h}{d_d} V_p v_d \quad (2.8)$$

and

$$F_{d2} = 2n_2\epsilon_0 \frac{h}{d_d} V_p v_d \quad (2.9)$$

where n_1 and n_2 are the numbers of fingers in each comb-drive electrode, V_p is the polarization voltage and v_d is the drive AC voltage.

2.3.2 Sense-Mode Design

Different from the comb-finger electrodes used in the drive-mode, the sense-mode uses parallel-plate electrodes to actuate and detect the proof masses' motion. Since the sense-mode is still a 2-DOF system, we can also simply regard its lumped element model as a 2-DOF mass-spring-damper system. Different from the drive-mode, an electrostatic stiffness k_e is being introduced into the system since the sense-mode oscillation is driven by parallel-plate electrodes. A noteworthy point is that an electrostatic spring-softening

effect is referred to k_e since it always reduces the mechanical stiffness, thus can be used for frequency tuning of the sense-mode. The definition of k_e is given by:

$$k_e = 2 \frac{C_s}{d_s^2} V_P^2 \quad (2.11)$$

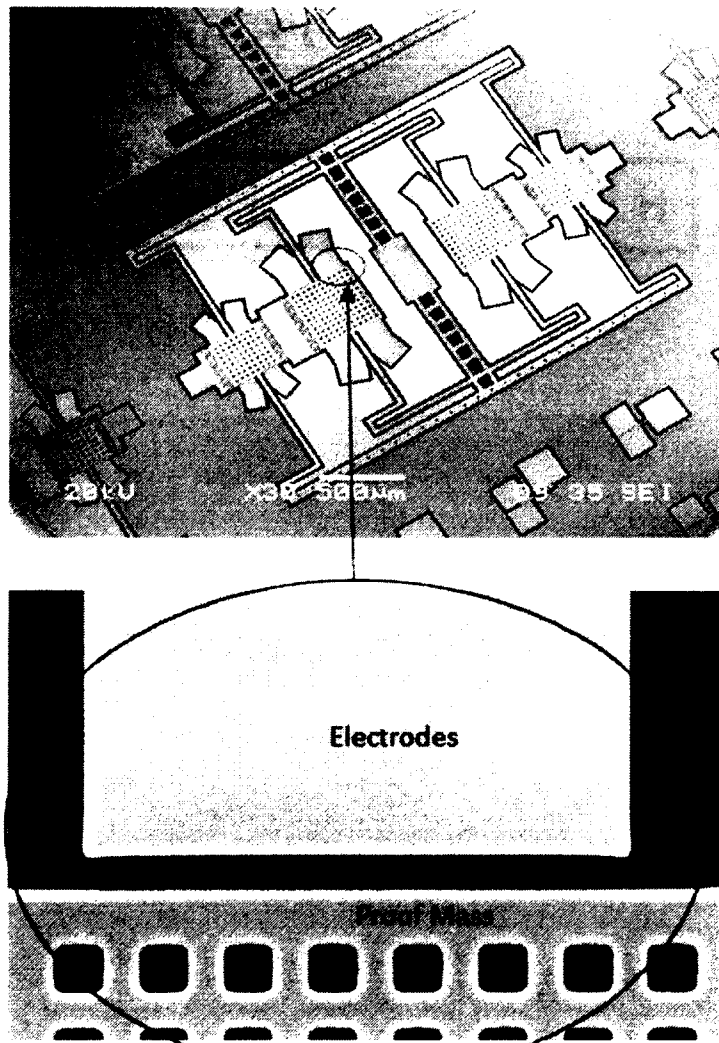


Figure 2.8: DRIE fabricated parallel-plate sense electrodes

Figure 2.8 shows a SEM picture of the parallel-plate electrodes in this TFG. For this particular design, two parallel-plate electrodes are employed for operating one proof mass. In reviewing of a single parallel-plate electrode, as shown in Fig. 2.8 and 2.9, the lower plate is just the proof mass while the upper plate is fixed on the substrate. When operating, a voltage difference is established between the two plates and the proof mass is vibrating thus changing the gap between the two plates, electrostatic force is generated and is given by:

$$F_e = \frac{1}{2} C_{s0} \frac{V^2}{d_s} + C_{s0} \frac{V^2}{d_s^2} y \quad (2.12)$$

where d_s is the sense gap, y is the displacement of the proof mass towards the upper plate and C_{s0} is the static sense capacitance.

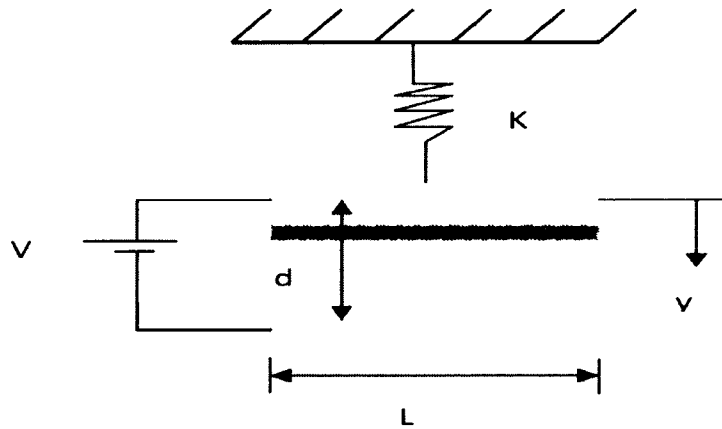


Figure 2.9: A schematic view of the parallel-plate electrostatic actuator

In reality, the parallel-plate electrodes are not used for actuation of the proof masses, but for sensing the capacitance change, in another word, current output, which is shown in Equation 2.13.

$$i_s = y_s \eta_s \omega_s = -\frac{C_{s0}}{d_s} V_p y_s \omega_s \quad (2.13)$$

where y_s is the displacement of the proof mass, C_{s0} is the capacitance between the two parallel-plate, Q_s is the sense-mode quality factor and ω_s is the angular resonant frequency of the sense-mode.

2.4 Design Configuration Type II

When considering the drive-mode quality factor and the sense-mode quality factor, it is obvious that the second one has more practical meaning than the first one since Q_s is directly related to the sense-mode vibration amplitude, hence, the mechanical sensitivity. In reviewing the design configuration type II, as shown in Fig. 2.10, the drive-mode motion is executed by parallel-plate electrodes while the sense-mode detector changes to comb-finger electrodes. Unlike previous tuning-fork implementations, the proposed architecture operates the linearly coupled, anti-phase resonant mode as the sense-mode, which prioritizes the sense-mode quality factor by minimizing the anchor loss in the sense direction [22]. The increasingly high quality factor in the sense-mode could provide a high mechanical sensitivity to the input angular rate through mode-matching when operated in vacuum.

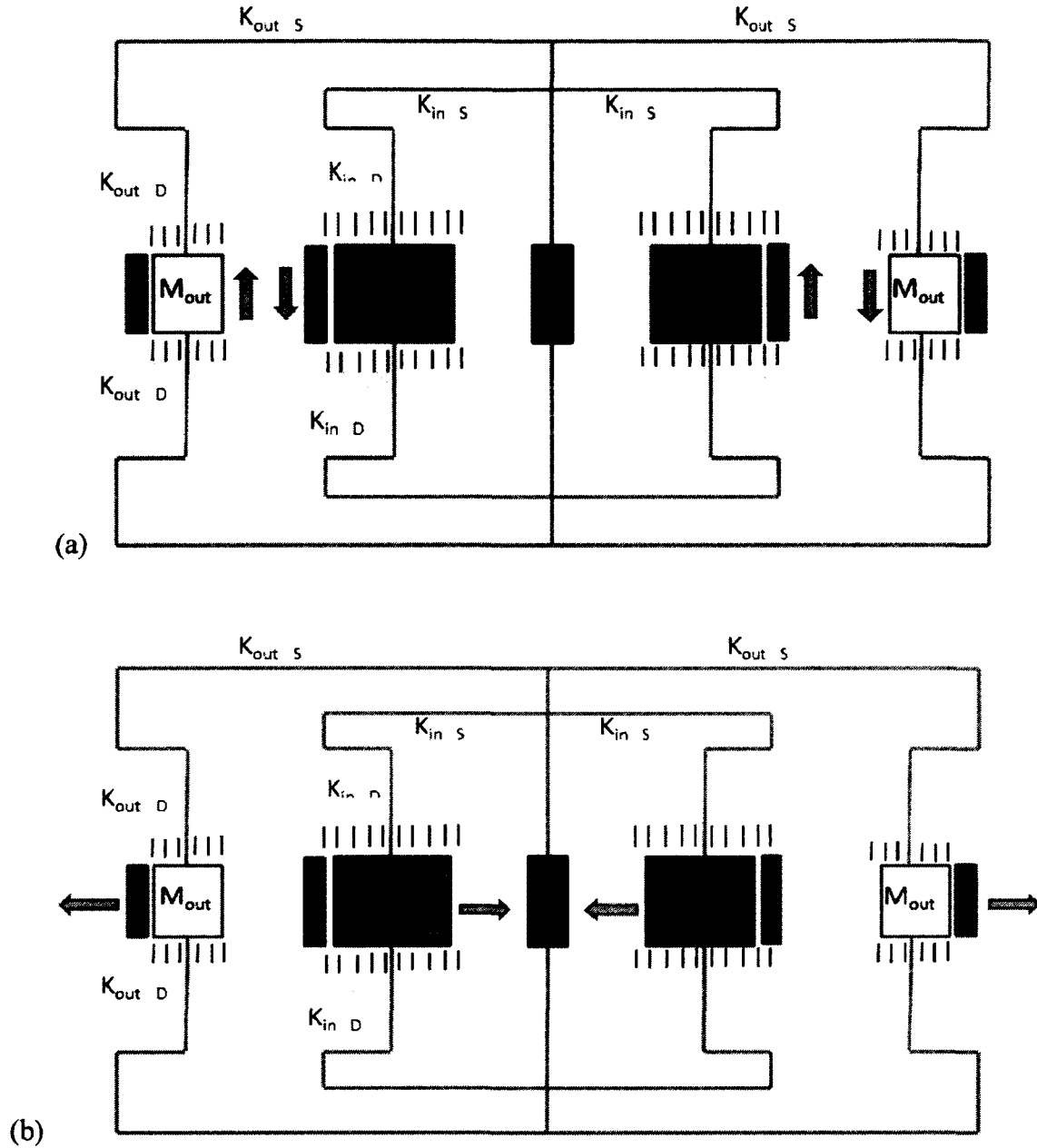


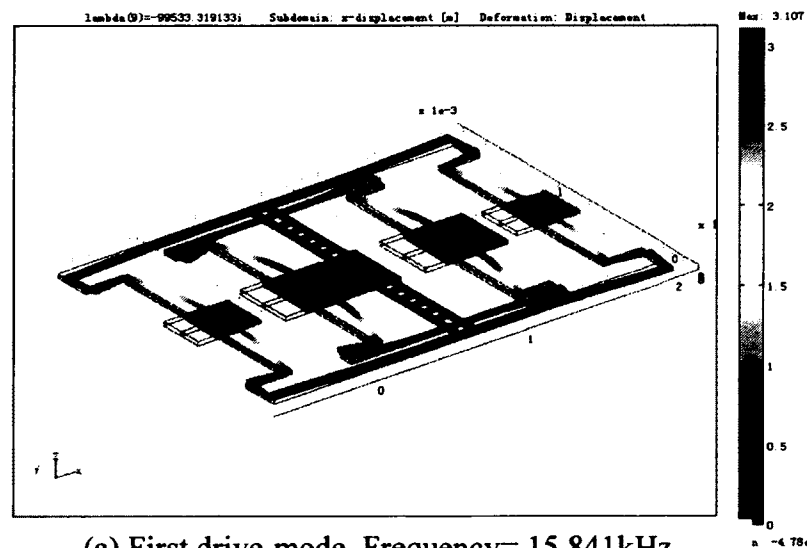
Figure 2.10: (a) Drive-mode motion and (b) Sense-mode motion

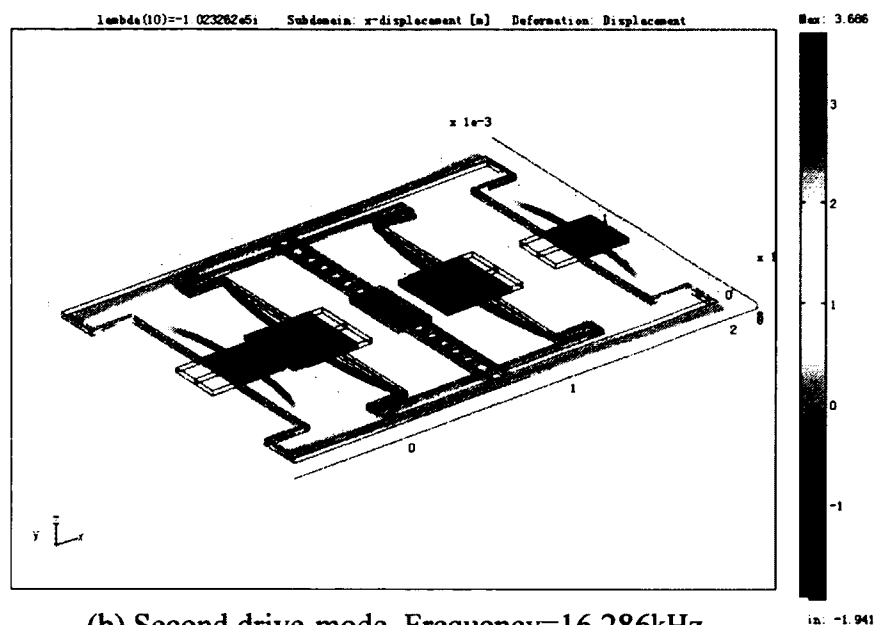
Comparing design configuration type I and type II, the mechanical structure is kept unchanged, which means the lumped element model and the governing equation are the same as discussed in Sections 2.3.1 and 2.3.2.

2.5 Finite Element Method Simulation

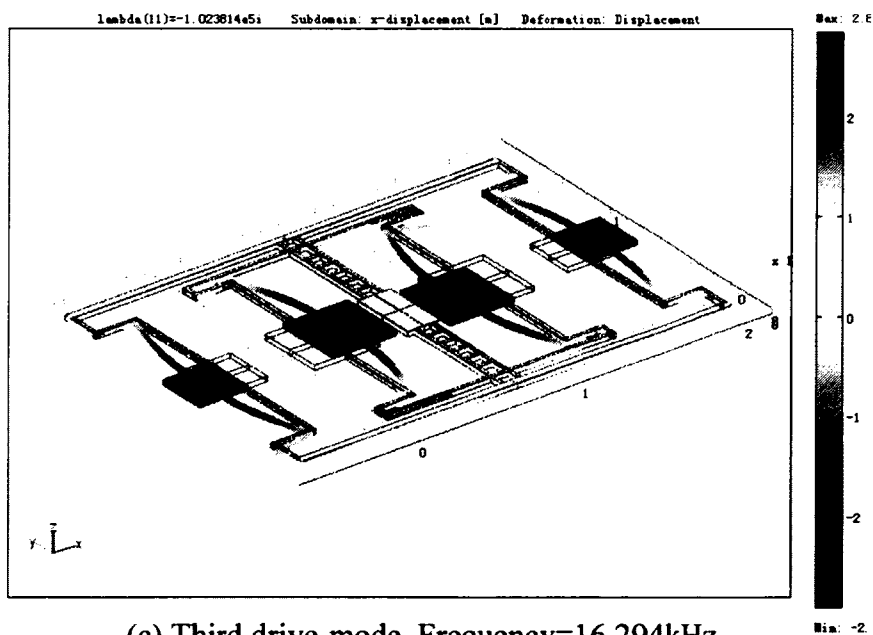
The purpose of carrying out the Finite Element Method (FEM) simulation of the prescribed structure is to look for the best design parameters which can satisfy the designated requirements. As mentioned before, the frequency of both the drive-mode and sense-mode should be larger than 10kHz but smaller than 20KHz to insure the robustness of the TFG against environmental noise. In addition, we recognize that the key parameters to control the frequency of the two vibration modes are the mechanical stiffness of the beams. Therefore, by conducting the FEM simulation, we can find the best value of the beam stiffness by optimizing the beam dimensions.

Theoretically, any mechanical structure could have an infinite number of modes from low frequency to high frequency. For this tuning-fork gyroscope, however, only the first eight in-plane modes are useful to be considered. Among these eight modes, as shown in Fig. 2.11, only the third drive-mode and the third sense-mode are the desired operational modes of the TFG.

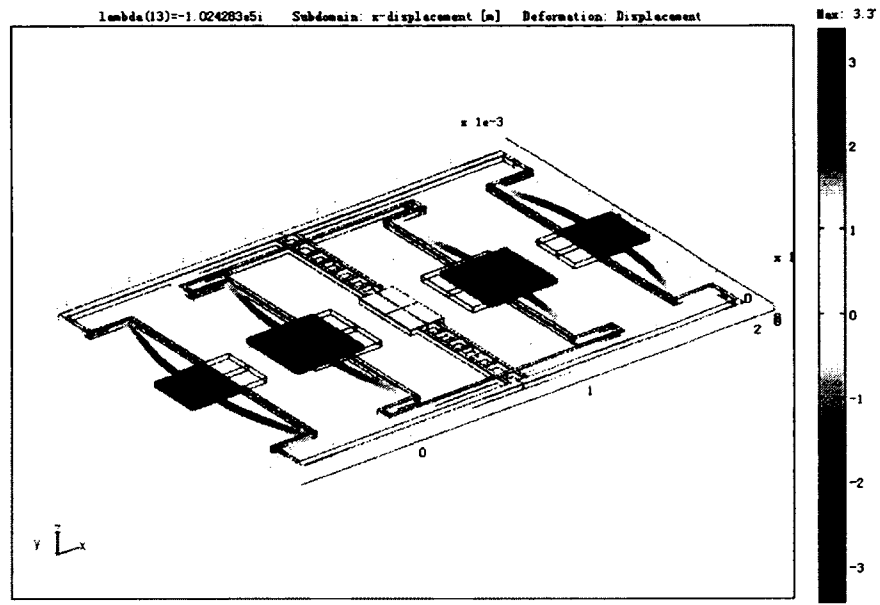




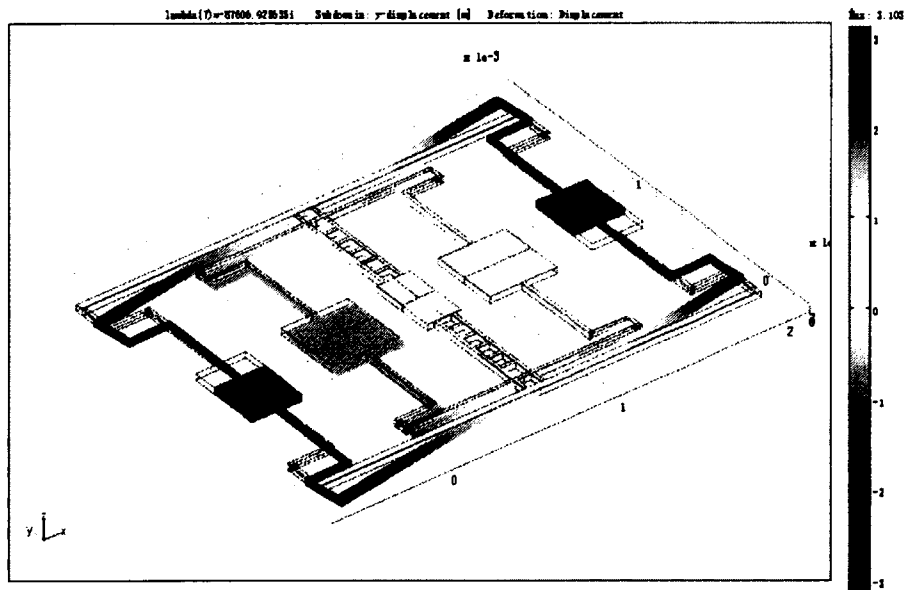
(b) Second drive-mode, Frequency=16.286kHz



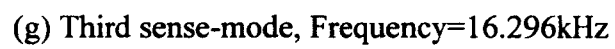
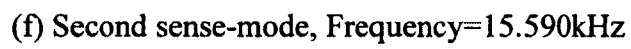
(c) Third drive-mode, Frequency=16.294kHz

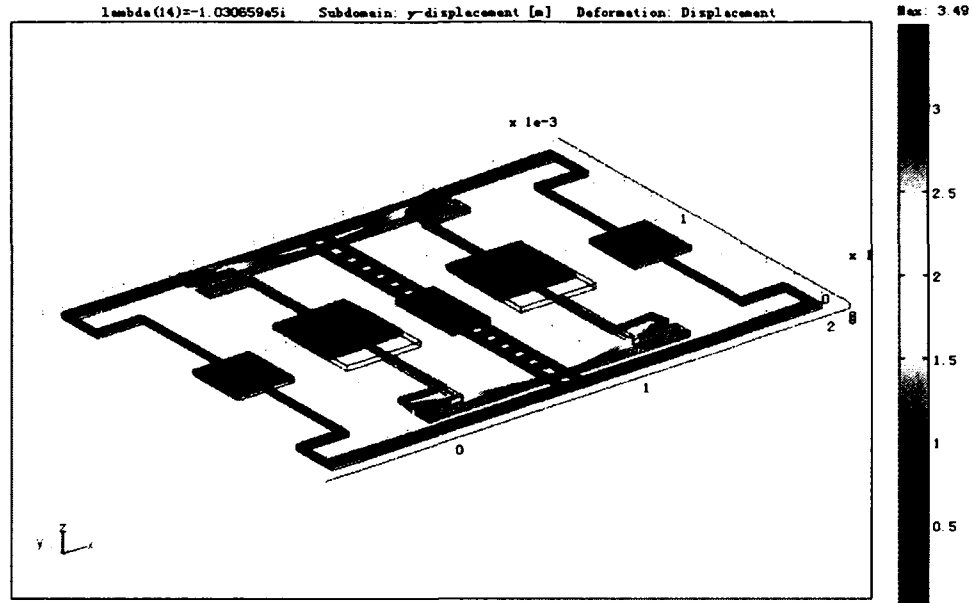


(d) Fourth drive-mode, Frequency=16.302kHz



(e) First sense-mode, frequency=13.943kHz





(h) Fourth sense-mode, Frequency=16.403kHz

Figure 2.11: FEM simulation results of the TFG

There are two basic requirements for the modes that need to be satisfied during the design process. The two modes should be contiguous and the sense-mode frequency should be slightly larger than the drive-mode frequency. Table 2.1 shows optimized mode order and their corresponding frequencies.

As shown in Table 2.1, the designated drive-mode frequency is 16.294kHz and the sense-mode frequency is 16.297kHz. They are the two neighboring modes with a small separation of 3 Hz, which satisfy the mode matching requirement.

Table 2.1: Simulation result of the TFG shows the frequency and mode order

Mode number	Frequency (KHz)	Mode type
1	13.943	Sense
2	15.590	Sense
3	15.841	Drive
4	16.286	Drive
5	16.294	Drive (desired)
6	16.297	Sense (desired)
7	16.302	Drive
8	16.403	Sense

CHAPTER 3

FABRICATION PROCESS

The tuning-fork gyroscope in this work is fabricated on the Silicon-On-Insulator (SOI) wafer using bulk micromachining technology. Only one mask is used in the entire fabrication process. The following paragraphs describe the fabrication procedure in detail.

3.1 Fabrication Procedure

Based on the design configuration presented in Chapter 2, the mask used for photolithography is designed using Computer Aided Design (CAD) software, where the dimensions of the structure are carefully mapped and the release holes are added. Fig. 3.1 shows the file used for making the TFG mask and Table 3.1 lists the dimension of the devices.

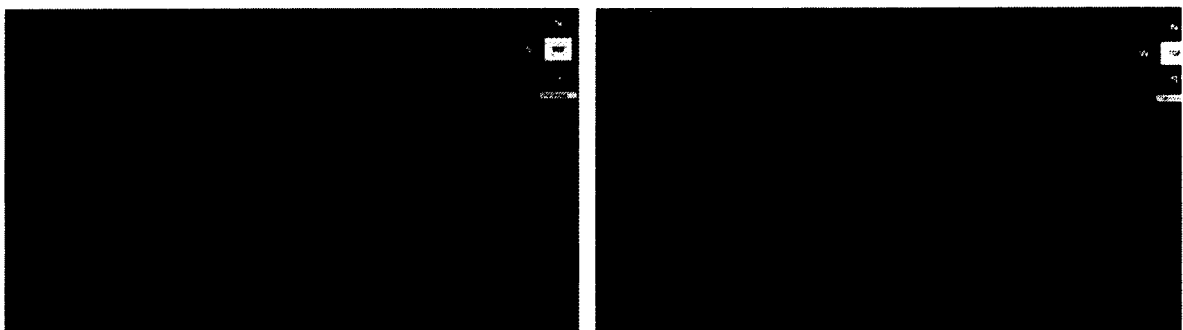


Figure 3.1: Mask drawing for the TFG

The TFG is fabricated on a SOI wafer, which has a $30\mu m$ thick heavily-doped device layer, a $2\mu m$ thick buried dioxide layer and a $300\mu m$ thick handle layer. The first step is

patterning the mechanical structures and transducers onto the device layer of the SOI wafer using Deep Reactive Ion Etching (DRIE) process. Different from wet chemical etching, DRIE is a dry etching technology developed for MEMS since it is a highly anisotropic etching process which could create high-aspect ratio trenches with vertical side walls [23, 24].

Table 3.1: Device dimensions in the mask file

Parameter	Value	Symbol	Units
Dimension of the device	2661×1936	-	μm^2
Beam width inner (drive)	22.5	B1	μm
Beam width outer (drive)	20.5	B2	μm
Beam width inner (sense)	21.5	B3	μm
Beam width outer (sense)	46.5	B4	μm
Beam length inner (drive)	1120	L1	μm
Beam length outer (drive)	1360	L2	μm
Beam length inner (sense)	1400	L3	μm
Beam length outer (sense)	2642	L4	μm
Small proof mass	300×300	S1	μm^2
Large proof mass	400×400	S2	μm^2
Release hole	15×15	R	μm^2

The time-controlled Hydrofluoric (HF) acid etching is followed to etch away silicon dioxide underneath the TFG, which allows the mechanical structure free to move. At the same time, the silicon dioxide under the anchor and the electrodes should be retained as much as possible with the purpose of holding them tightly on the substrate [25]. The DRIE process was conducted at Cornell Nanofabrication Facility (CNF) and the HF etching step is performed at the Micro Devices and Micromechanics Laboratory, Old Dominion University. Fig. 3.2 shows a schematic view of the fabrication process.

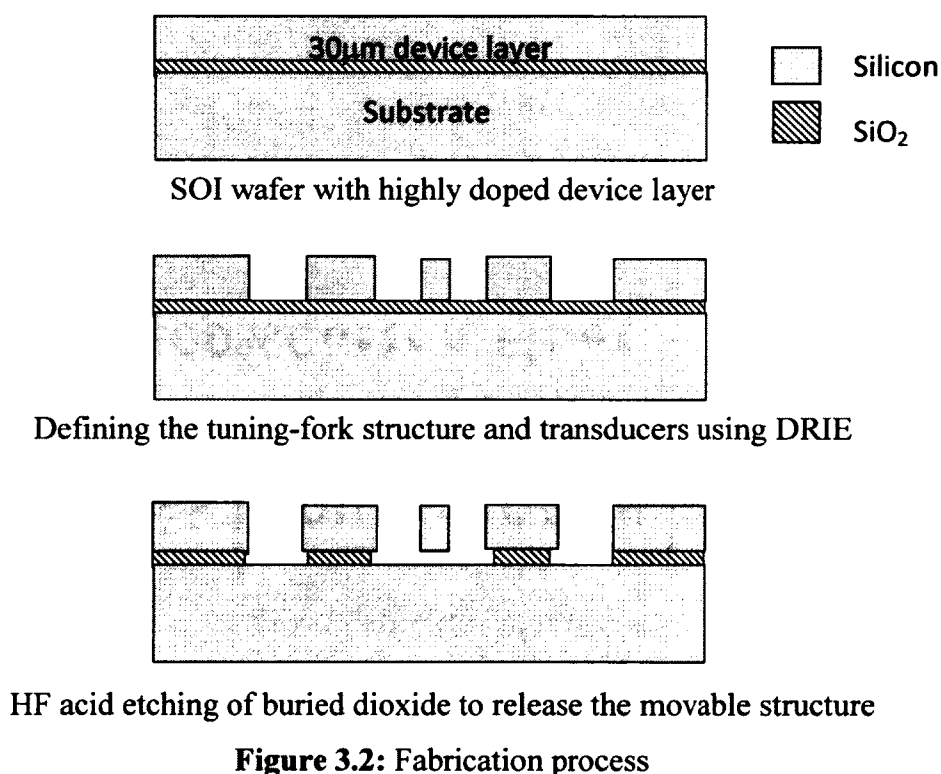


Fig. 3.3 shows the Scanning Electron Microscope (SEM) pictures of the fabricated device, which were taken by Dr. Wei Cao at the Applied Research Center, Old Dominion University.

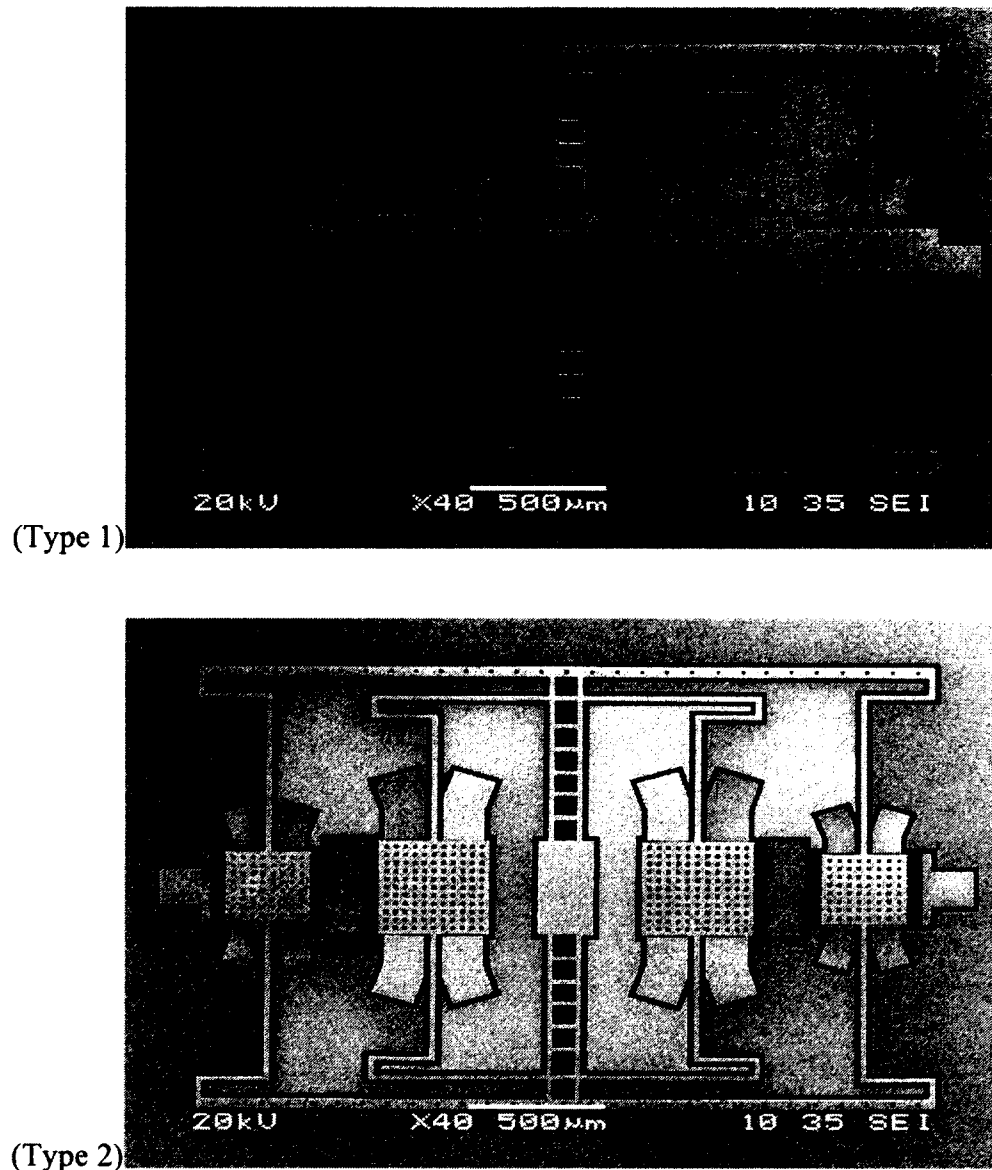


Figure 3.3: SEM picture of the fabricated TFG

A noteworthy point is that the smallest design feature of this TFG is the sensing gap between the sense electrode and proof mass, which is only $3\mu m$. The small gap is hard to be etched through by HF acid, since surface tension slows HF liquid to get into the gap. As a result, it usually takes a longer time for HF acid to etch through the gap so that extra

time used for etching the gap could cause over-etching of other parts of the TFG. Fig. 3.4 shows a close-up view of the sensing gap.

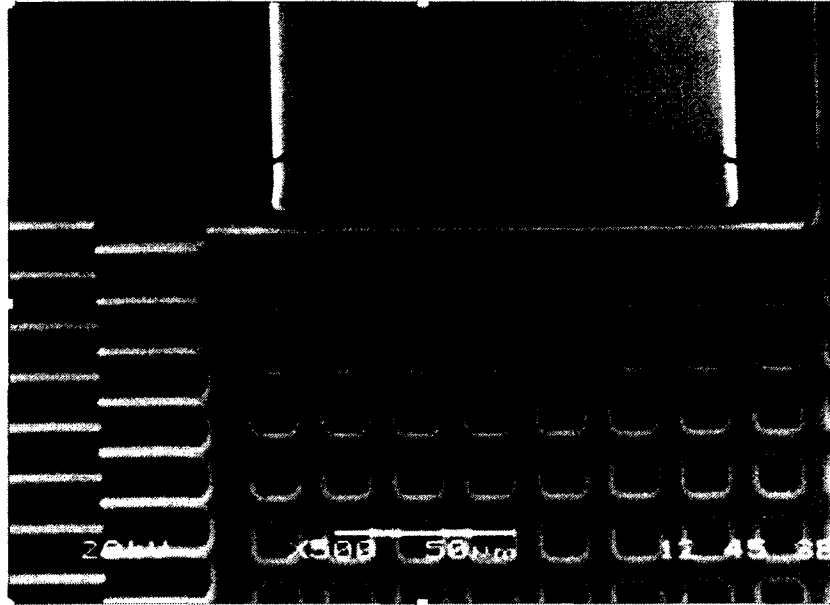


Figure 3.4: Sensing gap configuration

3.2 Fabrication Imperfections

Based on the discussions in Chapter 1, the mode-matching requirement renders the system response very sensitive to variations in parameters due to fabrication imperfections and fluctuations in operating conditions. Inevitable fabrication imperfections affect both the geometry and the material properties of MEMS devices. Among different kinds of issues, over-etching is identified as the most critical factor that affects the yield percentage of the fabrication process. In this one mask fabrication process, over-etching comes from both etching steps: one is DRIE over-etching and the other is HF acid over-etching. In some sense, some DRIE over-etching is tolerable since

it would allow all the mechanical structures to be completely patterned on the device layer, however, too much DRIE over-etching is harmful since it will induce fuzzy edges and undercutting of the structures. Fig. 3.5 shows the evidence of DRIE over-etching.

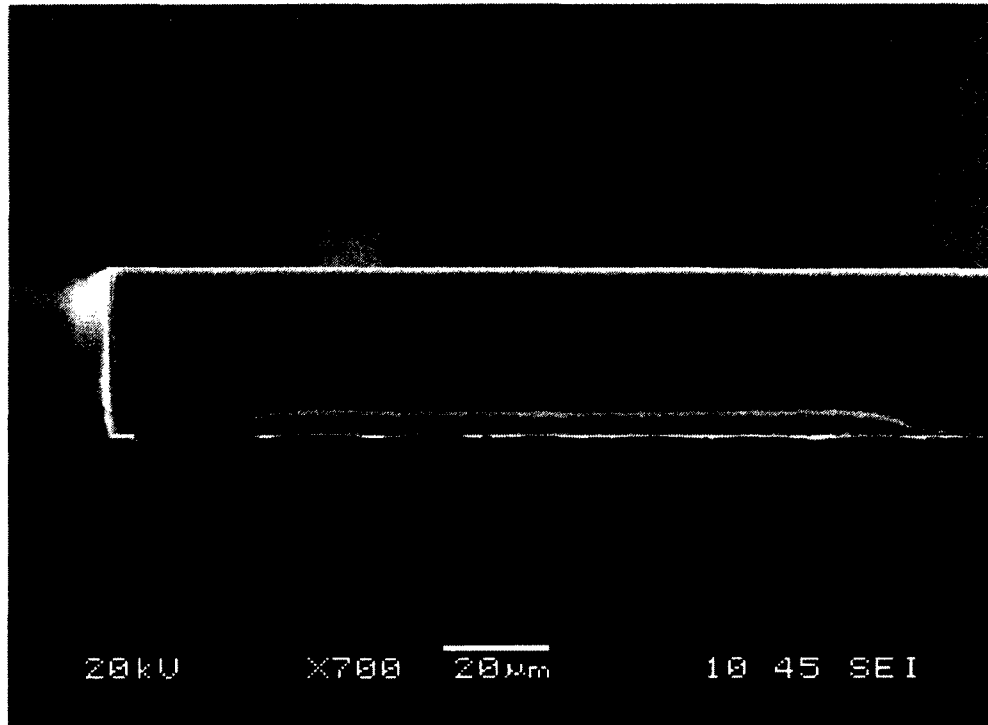


Figure 3.5: DRIE over-etching

Different from dry etching, HF etching is one kind of wet etching so that it etches away silicon dioxide isotropically. The HF over-etching under the anchor would induce an area change of the anchor foundation and thus make the anchor unstable. Likewise, the HF over-etching under the electrodes could cause them unsteady. When wire bonding process is being applied on the electrodes, they might not be able to hold tightly on the substrate and thus fall off and lose their function. Fig. 3.6 shows the consequences of HF over-etching.

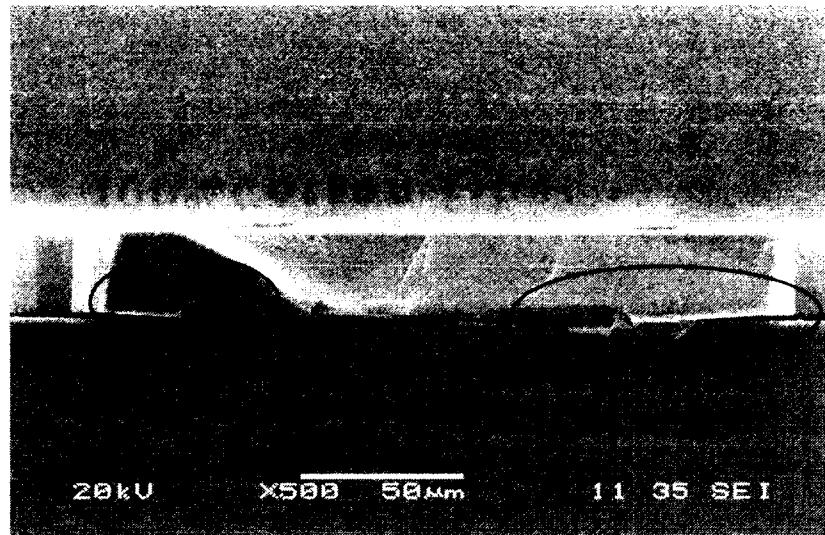


Figure 3.6: HF over-etching under the anchor

In summary, fabrication imperfections such as DRIE over-etching and HF over-etching make the system characteristics deviate drastically from the designed values. In some cases, this problem would cause the gyroscope system partially, or even completely fail. Thus, process control becomes extremely critical to minimize device-to-device, die-to-die, and wafer-to-wafer variations, and to realize a device with the desirable performance.

CHAPTER 4

EXPERIMENTAL CHARACTERIZATION

This chapter starts with analyzing the electromechanical system level model of the TFG. The experimental characterization technique for frequency response extraction is followed. Results from various experiments of the TFG are discussed.

4.1 Electromechanical System Level Model

In order to analyze and measure the performance of the tuning-fork gyroscope, the equivalent circuit model of the TFS should be characterized in the beginning. The tuning-fork gyroscope can be regarded as a coupled resonator system with the rotation induced Coriolis force being the coupling element between the two resonant modes [26]. The tuning-fork gyroscope mechanism can be translated to an equivalent circuit model with the purpose of electro-mechanical coupling. Table 4.1 lists the basic electrical analogy and the equivalent mechanical quantities.

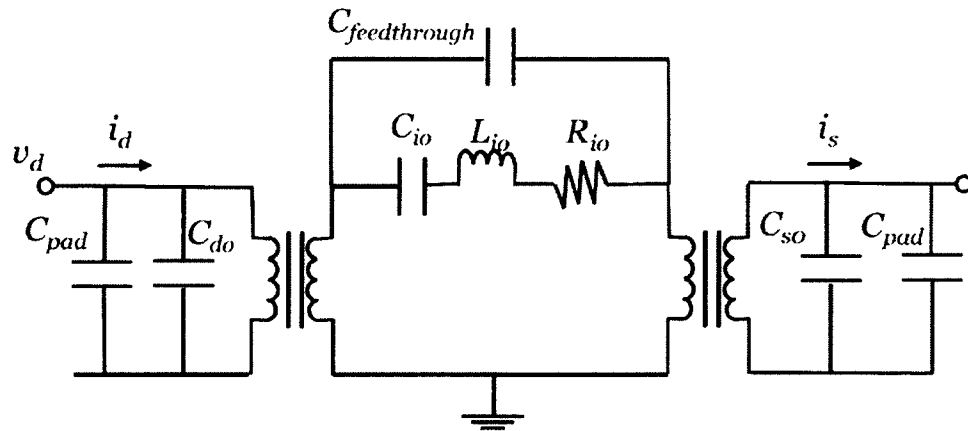


Figure 4.1: Equivalent electrical circuit model for a two port MEMS resonator

As shown in Fig. 4.1, the mechanical structure of the two port MEMS resonator is translated into a series RCL circuit, which can be incorporated into drive-loop electronic for operation.

Table 4.1: Basic electrical analogy and equivalent mechanical quantities

Electrical field	Electrical Symbol	Mechanical Field (Translation)	Mechanical symbol
Resistance (Ohm)	R	Damping Coefficient (kg/s)	D
Inductance (Henry)	L	Equivalent mass (kg)	m
Capacitance (F)	C	Reciprocal of stiffness $1/(\mu\text{N}/\mu\text{m})$	$\frac{1}{k}$
Voltage (V)	v	Electrostatic force (μN)	F
Current (A)	i	Displacement Velocity ($\mu\text{m}/\text{sec}$)	$\frac{dy}{dt}$
Charge (Q)	Q	Displacement (μm)	y

For the presented tuning-fork gyroscope, both comb-drive electrodes and parallel-plate electrodes (as shown in Fig. 4.2) are employed for operating the proof masses. The overall transfer functions of the comb-drive electrodes and parallel-plate electrodes are given by:

$$Y_{21-Comb}(j\omega) = \frac{I_{output}(j\omega)}{V_{input}(j\omega)} = \frac{(\frac{2\varepsilon \cdot n \cdot h}{d})^2 \cdot V_p^2}{M \cdot s + D + k/s} \quad (4.1)$$

and

$$Y_{21-para}(j\omega) = \frac{I_{output}(j\omega)}{V_{input}(j\omega)} = \frac{\frac{C_{d0}}{d_d} \cdot \frac{C_{s0}}{d_s} \cdot V_p^2}{M \cdot s + D + \frac{k - k_e}{s}} \quad (4.2)$$

where d_d is the gap between two parallel-plate of the input port and d_s is the gap between two parallel-plate of the output port, V_p is the polarization voltage applies on the device, n is the number of fingers of the comb-drive electrodes, ε is the electrical permittivity and h is the height of the fingers.

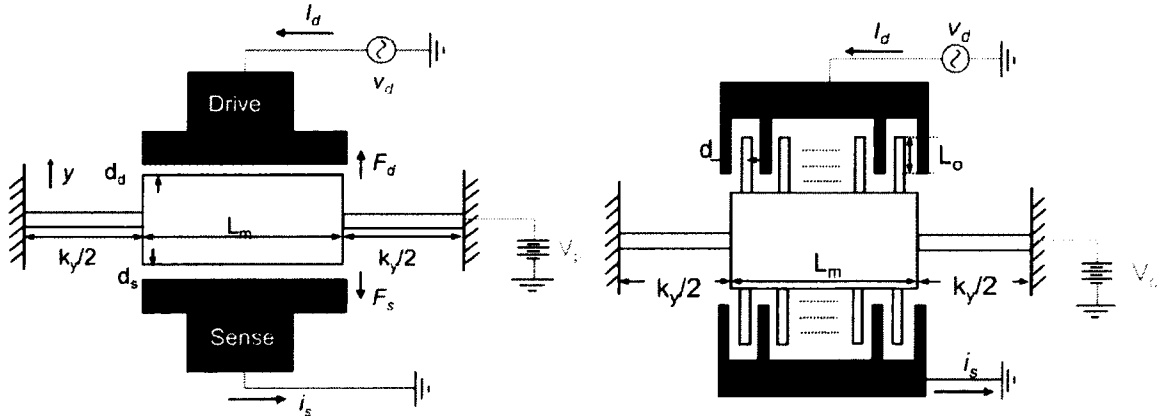


Figure 4.2: Schematic view of the two port resonator with parallel-plate (left) electrodes and comb-drive electrodes (right).

4.2 Experimental Setup for Q Measurement

Based on the previous work done by ODU MEMS group, a Trans Impedance Amplifier (TIA) with a feedback resistor is used for sensing of the motion current. TIA provides a low noise front end interface in both the drive and sense capacitance detection [27]. In comparison of the electrical system and mechanical system, the definitions of quality factor of two different forms are given by Equations 4.3 and 4.4:

$$Q = \frac{1}{R} \sqrt{\frac{L}{C}} \quad (4.3)$$

$$Q = \frac{1}{D} \sqrt{mk} \quad (4.4)$$

Equation 4.3 shows the definition of quality factor in a RCL circuit, which is the equivalent circuit model of the TFS. As electrical components, the inductor stores energy as a magnetic field and the capacitor stores energy in the form of charge, while resistor dissipates energy in the form of heat. Similar as the RCL circuit, Equation 4.4 shows the similar energy transfer analogy for the lamped mechanical system. The moving mass and deformed spring serve as the energy storage mechanism while damper is the energy dissipation mechanism.

The frequency response measurement is performed to find out the resonant frequencies and the quality factors of the drive-mode and sense-mode. Figs. 4.3 and 4.4 show a schematic view and pictures of the experimental setup for measuring the frequency response of a TFG.

In the beginning, a die of gyroscopes is fixed on a PCB and a gyroscope is wire-bonded to the copper pads that are connected to a TIA front-end with a feedback resistor of $R_F = 5.1\text{M}\Omega$. The PCB is then placed in a vacuum chamber and electrically connected to other instruments. A network analyzer, a DC supply and an AC supply are employed to operate the gyroscope system. With a polarization voltage V_p applied on the anchor, an AC drive voltage V_{in} is applied on one electrode, and then a sense current signal I_{out} can be detected from the other electrode, which is further converted into a voltage through the TIA front-end.

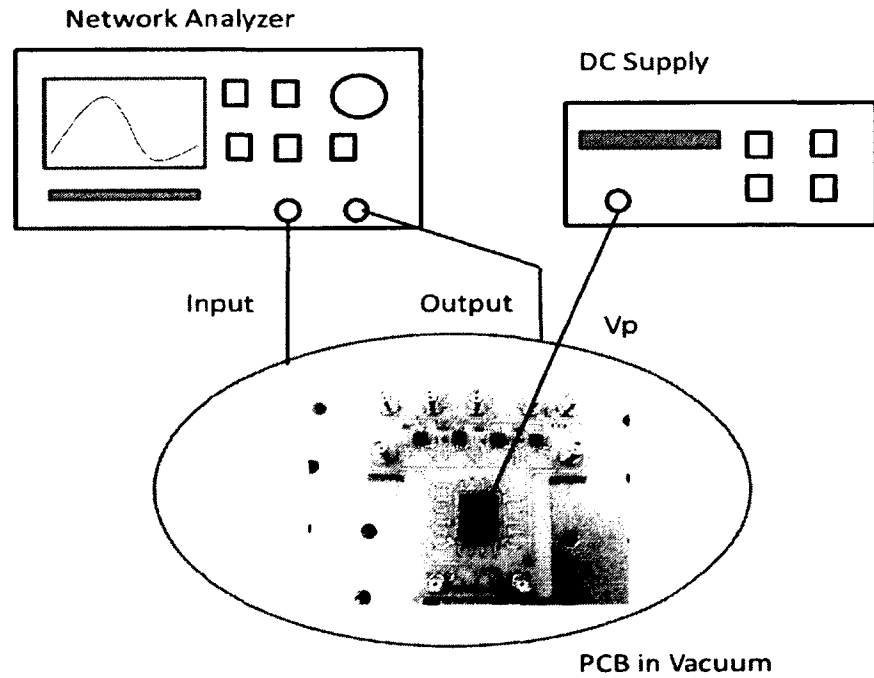


Figure 4.3: Schematic view of experimental setup

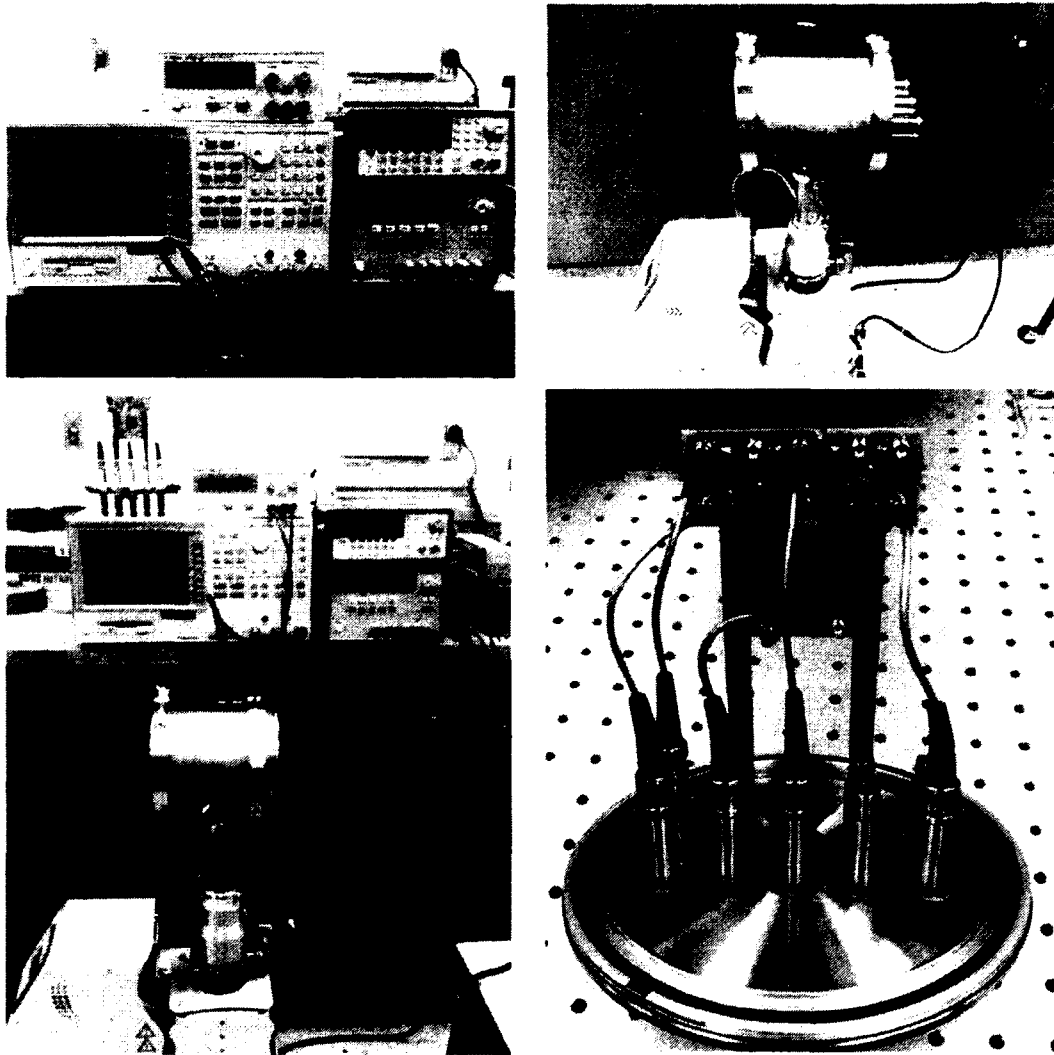


Figure 4.4: Testing equipment and setup

4.3 Testing Results and Discussions

Five devices are measured and the results are shown in Table 4.2. The resonant frequencies of the actual fabricated devices are slightly different from one to another since the wafers have gone through different DRIE loops, which reflect in various structural dimensions.

Table 4.2: Testing results of the fabricated devices

Device#	Drive-mode		Sense-mode	
	Frequency (KHz)	Q (K)	Frequency (KHz)	Q (K)
#1	18.73975	3.7916	19.62775	2.1835
#2	19.19125	24.43	19.69395	25.822
#3	19.22175	2.1387	19.6589	29.75
#4	19.262	8.3413	19.6597	21.202
#5	19.33745	16.356	19.5482	39.768

In reviewing the testing results, the drive-mode resonant frequencies are in the range of 18.74kHz to 19.34kHz and the sense-mode resonant frequencies are in between 19.54kHz and 19.69kHz. Base on the data, we can conclude that the sense-mode quality factor is no less than the drive-mode quality factor, which proves the design optimization idea. The original measured graphs of Device #2 and #4 are shown in Fig. 4.5.

Several problems could be seen from the testing results. In the first place, the drive-mode and sense-mode resonant frequencies have a large separation (300Hz-900Hz), which is caused by the variation of beam dimensions. During the design process, the beam length and width are optimized well enough to make the two modes close to each other. When carrying out the mask drawing and the fabrication process, due to structural variation and fabrication imperfections, the resonant frequencies are inevitably changed

to some extent. This problem can be further eliminated by iterating the design and fabrication process of the device. Secondly, even though the sense-mode quality factor is larger than the drive-mode quality factor, the absolute values of the quality factors of both modes are not as good as the first generation TFG. One reason is that the beams of this gyroscope are not the same as the multiple-parallel structure used in the previous TFG, which is proved to be more effective in reducing TED. Another reason is that the dimension of this TFG is doubled compare to the first generation TFG, so that the energy dissipation would be much larger.

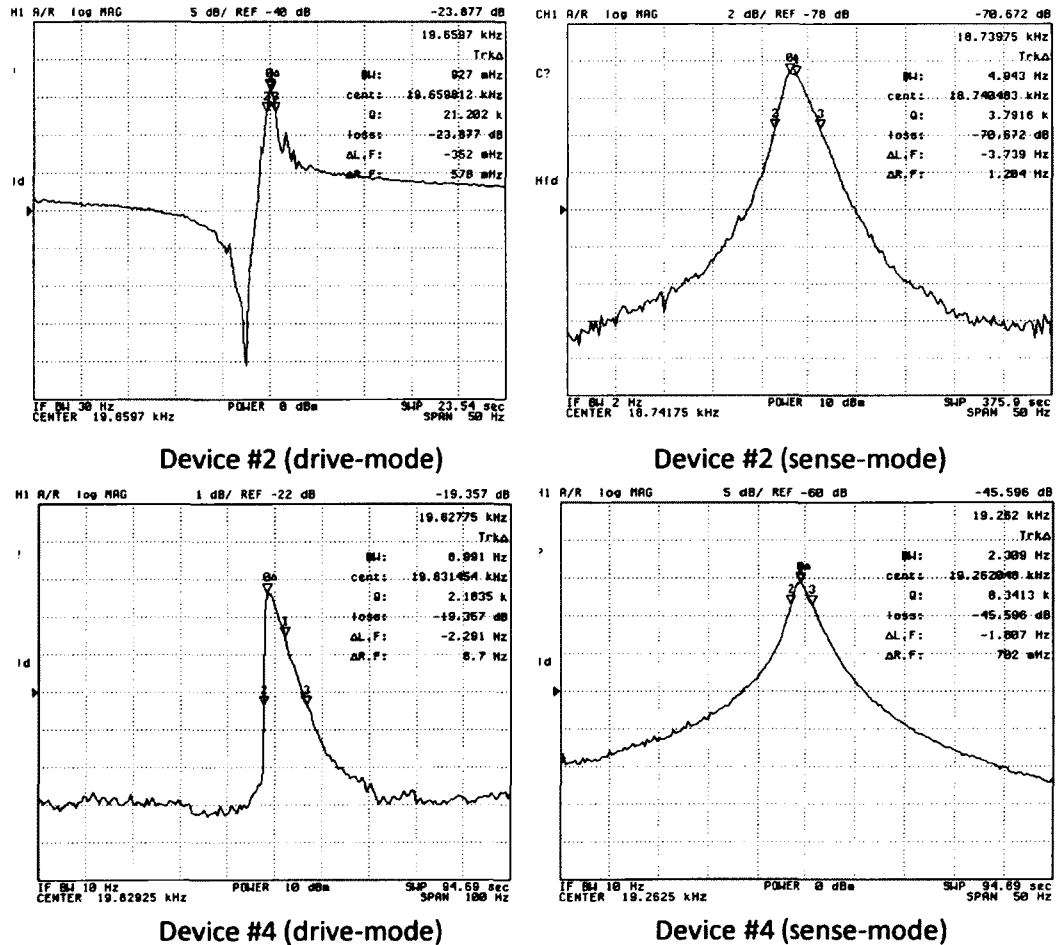


Figure 4.5: Measured frequency response for Device #2 and #4

CHAPTER 5

CONCLUSIONS AND FUTURE DIRECTIONS

5.1 Summary of the Research Work

This thesis focuses on the design, modeling, and experimental characterization of a MEMS tuning-fork gyroscope. First of all, the technical limitations of a current developed tuning-fork gyroscope are analyzed in order to address new optimization methods. Then, a new tuning-fork gyroscope structural improvement is presented with the purpose of balancing the net torque in the sense-mode. Theoretical calculations and FEM simulations are conducted to further proof the design idea. The dimension of the structure is being optimized based on the designated vibration mode order and mode shape using Comsol Multiphysics. In addition, the mask is created using CAD software for the four inch silicon wafer. The silicon wafer is then fabricated at the Cornell Nanofabrication Facility using DRIE. HF acid etching and wafer post processing is done in the Micro Device Laboratory at Old Dominion University. Meanwhile, frequency response testing is conducted to measure the devices' natural frequencies and corresponding quality factors in both drive-mode and sense-mode. Five different devices are measured with the results of improved quality factor in the sense-mode, which proved the design concept.

5.2 Future Direction

Several future directions can be followed to further improve the performance of this TFG. These paths are briefly discussed below.

(1) In this work, the frequency separation between drive-mode and sense-mode is relatively large due to fabrication imperfections, which does not fit the designed value and the mode-matching requirement. This problem can be resolved by optimizing the mask layout of the TFG, in other words, by assigning the devices' dimensions within a small range instead of a specific value. This will ensure a certain yield percentage of the silicon wafer, hence, some working devices.

(2) In this work, the performance of the device varies greatly from one to another since the fabrication imperfections are hard to control. This problem could be fixed either by applying different fabrication procedures or by using more advanced etching equipment.

(3) In addition to quality factor, parameters such as rate sensitivity, bandwidth and angle random walk are hard to be characterized in this work since the lack of fully functional devices. This could be solved by iterating the design, fabrication and testing process until all the problems are resolved.

REFERENCES

- [1] E. Gusev, E. Garfunkel, A. Dideikin, and SpringerLink (Online service). (2010). *Advanced Materials and Technologies for Micro/Nano-Devices, Sensors and Actuators*. Available: <http://dx.doi.org/10.1007/978-90-481-3807-4>
- [2] M. N. Armenise, C. Ciminelli, F. Dell'Olio, V. M. N. Passaro, and SpringerLink (Online service). (2011). *Advances in Gyroscope Technologies*. Available: <http://dx.doi.org/10.1007/978-3-642-15494-2>
- [3] S. Merhav, *Aerospace sensor systems and applications*. New York: Springer, 1996.
- [4] D. Piyabongkarn and R. Rajamani, "The development of a MEMS gyroscope for absolute angle measurement," *American Control Conference, 2002*. pp. 1960-1965 vol.3.
- [5] P. Zhang, J. Gu, E. E. Milios, and P. Huynh, "Navigation with IMU/GPS/digital compass with unscented Kalman filter," in *Mechatronics and Automation, 2005 IEEE International Conference*, 2005, pp. 1497-1502 Vol. 3.
- [6] C. Jekeli, *Inertial navigation systems with geodetic applications*. Berlin; New York: Walter de Gruyter, 2001.
- [7] R. Wang, "Interface Circuit for a Multiple-Beam Tuning-fork Gyroscope with High Quality Factor," Ph.D dissertation, Department of Mechanical Engineering, Old Dominion University, Norfolk, 2011.
- [8] J. Bernstein, S. Cho, A. T. King, A. Kourepenis, P. Maciel, and M. Weinberg, "A micromachined comb-drive tuning fork rate gyroscope," in *Micro Electro Mechanical Systems, 1993, MEMS '93, Proceedings An Investigation of Micro Structures, Sensors, Actuators, Machines and Systems. IEEE.*, 1993, pp. 143-148.
- [9] C. Acar, A. Shkel, and SpringerLink (Online service). (2009). *MEMS Vibratory Gyroscopes Structural Approaches to Improve Robustness*. Available: <http://dx.doi.org/10.1007/978-0-387-09536-3>
- [10] K. Sahin, E. Sahin, S. E. Alper, and T. Akin, "A wide-bandwidth and high-sensitivity robust microgyroscope," *Journal of Micromechanics and Microengineering*, vol. 19, Jul 2009.
- [11] "IEEE Standard for Inertial Systems Terminology," *IEEE Std 1559-2009*, pp. c1-30, 2009.

- [12] S. Ajit, "CMOS systems and circuits for sub-degree per hour MEMS gyroscopes," Ph.D. dissertation, Electrical and Computer Engineering, Georgia Institute of Technology, Atlanta, 2007.
- [13] A. A. Trusov, A. R. Schofield, and A. M. Shkel, "Performance characterization of a new temperature-robust gain-bandwidth improved MEMS gyroscope operated in air," *Sensors and Actuators A: Physical*, vol. 155, pp. 16-22, 2009.
- [14] K. Sahin, E. Sahin, S. E. Alper, and T. Akin, "A wide-bandwidth and high-sensitivity robust microgyroscope," *Journal of Micromechanics and Microengineering*, vol. 19, p. 074004, 2009.
- [15] V. Kempe, *Inertial MEMS: Principles and practice*. Cambridge ; New York: Cambridge University Press, 2011.
- [16] R. Wang, P. Cheng, F. Xie, D. Young, and Z. Hao, "A multiple-beam tuning-fork gyroscope with high quality factors," *Sensors and Actuators A: Physical*, vol. 166, pp. 22-33, 2011.
- [17] J. H. Harlow, *Electric power transformer engineering*. Boca Raton: CRC Press, 2004.
- [18] Y. Xu, R. Wang, S. K. Durgam, Z. Hao, and L. Vahala, "Numerical models and experimental investigation of energy loss mechanisms in SOI-based tuning-fork gyroscopes," *Sensors and Actuators A: Physical*, vol. 152, pp. 63-74, 2009.
- [19] M. F. Zaman, A. Sharma, H. Zhili, and F. Ayazi, "A Mode-Matched Silicon-Yaw Tuning-Fork Gyroscope With Subdegree-Per-Hour Allan Deviation Bias Instability," *Journal of Microelectromechanical Systems*, vol. 17, pp. 1526-1536, 2008.
- [20] S. D. Senturia and NetLibrary Inc. (2001). *Microsystem design*. Available: <http://www.netLibrary.com/urlapi.asp?action=summary&v=1&bookid=78508>
- [21] H. Zhili, "Micro Devices lecture notes," Department of Mechanical and Aerospace Engineering, Old Dominion University, Norfolk, 2011.
- [22] A. A. Trusov, I. P. Prikhodko, S. A. Zotov, A. R. Schofield, and A. M. Shkel, "Ultra-high Q silicon gyroscopes with interchangeable rate and whole angle modes of operation," in *Sensors, 2010 IEEE*, 2010, pp. 864-867.
- [23] National Research Council (U.S.). Committee on Advanced Materials and Fabrication Methods for Microelectromechanical Systems. and NetLibrary Inc., "Microelectromechanical systems advanced materials and fabrication methods," ed. Washington, DC: National Academy Press, 1997.

- [24] V. Lindroos, A. Lehto, T. Motooka, and M. Tilli. (2010). *Handbook of Silicon Based MEMS Materials and Technologies*. Available: <http://www.columbia.edu/cgi-bin/cul/resolve?clio8569433>
- [25] J. A. Geen, S. J. Sherman, J. F. Chang, and S. R. Lewis, "Single-chip surface micromachined integrated gyroscope with 50deg/h Allan deviation, *IEEE Journal of Solid-State Circuits*, vol. 37, pp. 1860-1866, 2002.
- [26] F. Ayazi and K. Najafi, "Design and fabrication of high-performance polysilicon vibrating ring gyroscope", *The Eleventh Annual International Workshop*, pp. 621-626, 1998
- [27] C. T. Nguyen, "Micromechanical Signal Processor," Ph.D dissertation, University of California, Berkeley, 1994.

VITA

Yujie Zhang received his B.S. degree in Mechanical Engineering from Shenyang University of Science and Technology, China in 2010. He is currently a graduate student in the Department of Mechanical and Aerospace Engineering, Old Dominion University, Norfolk, VA, USA. His research interests are design MEMS inertial sensors and other MEMS based devices.